

Donor-based qubits for quantum computing in silicon

Cite as: Appl. Phys. Rev. **8**, 031314 (2021); doi: [10.1063/5.0060957](https://doi.org/10.1063/5.0060957)

Submitted: 23 June 2021 · Accepted: 10 August 2021 ·

Published Online: 15 September 2021



View Online



Export Citation



CrossMark

J. C. McCallum,^{1,a)}  B. C. Johnson,²  and T. Botzem³ 

AFFILIATIONS

¹School of Physics, University of Melbourne, Melbourne, Victoria 3010, Australia

²Centre for Quantum Computation and Communication Technology, School of Engineering, RMIT University, Melbourne, VIC 3001, Australia

³Centre for Quantum Computation and Communication Technology, School of Electrical Engineering and Telecommunications, UNSW Sydney, Sydney, NSW 2052, Australia

Note: This paper is part of the Special Topic on Quantum Computing.

^{a)}Author to whom correspondence should be addressed: jeffreym@unimelb.edu.au

ABSTRACT

Spin-qubits based on impurities such as phosphorus in silicon (Si) have attractive attributes for the development of quantum computing devices. Very long coherence times can be achieved for donor-based qubits in Si due to the availability of isotopically pure ²⁸Si layers where the ²⁹Si atoms, which otherwise lead to decoherence, are largely absent in the active region of the device. Well-behaved single donor qubits in Si can routinely be formed using ion implantation, and the key performance criteria needed to demonstrate the basis of a viable platform for quantum computing have been achieved. The crucial next stage of development is to demonstrate suitable pathways for scale-up that allow patterned arrays of donor qubits to be controllably coupled and that are robust against the inherent donor placement tolerances and material processing constraints that exist. Here, we review progress on the fabrication and measurement of donor-based qubits in silicon via the ion implantation pathway and discuss the key developmental milestones that have been achieved. We also provide an overview of the key scale-up strategies that are being actively pursued to take donor-based quantum computing in Si to the next stage.

Published under an exclusive license by AIP Publishing. <https://doi.org/10.1063/5.0060957>

TABLE OF CONTENTS

I. INTRODUCTION	1	1. Atom counting	16
II. DONOR-BASED QUBITS IN SILICON	2	2. Spatial control	16
A. Phosphorus donor qubits	3	D. Summary	16
B. P-donor qubits: Electron spin initialization and control	4	IV. IMPLANTATION SCALE-UP PATHWAYS	17
C. P-donor qubits: Nuclear spin initialization and control	5	A. <i>J</i> -coupled qubits	17
D. P-donor qubits: Isotopically engineered ²⁸ Si epilayers	7	B. Flip flop qubit	18
E. P-donor qubits: Stark-tuning	8	1. Coupling to microwave photons	19
F. P-donor qubits: Dressed states	8	C. Additional couplings strategies	20
G. P-donor qubits: Coupled qubits	9	1. Donor spin qubit architectures	20
H. Donors other than phosphorus	12	2. Spin chains	20
1. Summary	13	3. Ferromagnets	20
III. DONOR QUBIT FABRICATION BY ION IMPLANTATION	13	4. Intermediate quantum dots	20
A. Ion implantation	13	D. Summary	20
B. Post-implant processing	14	V. CONCLUSIONS	21
C. Deterministic ion implantation	15		
		I. INTRODUCTION	
		Quantum computers offer key advantages over conventional computers for solving some important classes of problems, and they provide entirely new functionality in areas like quantum cryptography	

that have no classical counterpart.^{1,2} From a scientific standpoint, one of the key advantages that quantum computing may offer is the potential to model quantum systems, with applications in quantum chemistry and drug design, for example.^{3–5} The fundamental building block of a quantum computer, the analog of the bit in a conventional computer, is the quantum bit or qubit. Over the past decade, intensive research has led to the experimental realization of qubits in a number of different systems including ion traps,⁶ superconducting circuits,⁷ and spins in semiconductors.⁸ For a quantum computer architecture to be viable, there are some stringent conditions that must be met. The qubits must be sufficiently isolated from their environment, and the quantum operations must be controllable, while the gate operation speed is sufficient to allow computations to be completed before decoherence and loss of quantum information occurs. Also, it must be possible to implement quantum error correction protocols, and the qubit architecture must be scalable. Some solid-state systems offer the prospect of being able to address these challenges, and considerable progress has been made on the implementation of qubits in silicon, semiconductor heterostructures, and diamond.^{8–13}

Spin-qubits based on impurities such as phosphorus in silicon are particularly attractive because of the vast knowledge of silicon (Si) processing that exists and because Si can be isotopically purified to eliminate the ²⁹Si, which otherwise leads to decoherence. Solid-state coherence times longer than 180 s have been demonstrated for a dilute ensemble of ³¹P in isotopically purified ²⁸Si.¹⁴ These coherence times are comparable to the longest times measured for isolated atoms and ions in vacuum. Coherent manipulation of both the electron¹⁵ and the nuclear¹⁶ spin of a single ³¹P donor has been demonstrated along with electrical readout of the spin state in single-shot mode with high fidelity. In addition, qubit–qubit coupling and two-qubit controlled gate operations have also been achieved recently.¹⁷

There are two main pathways to develop donor-based qubits in Si. One approach utilizes the Si semiconductor industry standard device processing technique of ion implantation, albeit at very low fluences, to introduce individual or small numbers of donors into the near surface region of a metal-oxide semiconductor device structure. Electron-beam lithographic patterning and processing is then employed to define gates and other device structures in close proximity to the implanted donor(s).^{18,19} The other approach combines the ability of the scanning tunneling microscope (STM) to probe and manipulate atoms at surfaces with a lithographic process that involves a hydrogen resist combined with phosphorus-doping to pattern and fabricate device structures with atomic resolution.^{20,21} These two approaches have very different attributes that dictate the possible pathways to qubit fabrication and to device scale-up. Here, we focus on the ion implantation approach to the fabrication of donor-based qubits in Si. We present the milestones that have been achieved and the near-term plans to develop suitable architectures for scale-up. Recent progress on the STM pathway to qubit development can be found in Refs. 22 and 23. Other recent reviews of qubits in Si include Refs. 24–27. Theoretical considerations relating to donor qubits in Si can be found in Refs. 28–30. Finally, Si-based quantum dots represent another important pathway that is being actively pursued, and recent works that cover this area of research include Refs. 31–33.

The remainder of this article is structured as follows: Sec. II provides an overview of the key milestones that have been achieved in the development of donor-based qubits in Si. Section III discusses the

particular attributes of the ion implantation process that make this particular pathway to development possible and also the constraints that need to be addressed for a viable scale-up pathway to exist. Section IV reviews current research on scale-up pathways for qubits in Si and Sec. V summarizes progress and future directions.

II. DONOR-BASED QUBITS IN SILICON

As early as 1959 in a now famous talk titled, “There’s Plenty of Room at the Bottom,” Feynman articulated a vision for the manipulation and control of matter at the atomic scale.³⁴ To quote just two statements from the talk, “When we get to the very, very small world—say circuits of seven atoms—we have a lot of things that could happen that represent completely new opportunities for design” and, “We can use not just circuits, but some system involving the quantized energy levels, or the interactions of quantized spins, etc.” This represents an early vision for the manipulation and control of matter at the level of individual atoms that would eventually evolve into quantum computing research. Feynman further updated this vision in 1982 in a paper titled “Simulating Physics with Computers.”³⁵ However, it was many years after the original vision before technological and theoretical capabilities were sufficiently well evolved to begin to make that vision a reality. For example, gate-defined III–V quantum dot devices emerged in the 1990s.³⁶ At the beginning of the 21st century, global interest in quantum computing began to grow rapidly, and there were many more ideas for possible qubits and qubit architectures than there was knowledge of how to build and operate such devices. In the year 2000, DiVincenzo provided some focus for the research that followed by defining a set of five requirements that a candidate system would have to be able to meet in order to yield a viable quantum computing platform.² The five requirements are as follows:

1. A scalable physical system with well-characterized qubits.
2. The ability to initialize the qubits to a simple fiducial state, such as $|0000\dots\rangle$.
3. Long relevant coherence times, much longer than the gate operation times.
4. A universal set of quantum gates.
5. A qubit-specific measurement capability.

DiVincenzo added two further requirements needed for quantum communications:

1. The ability to interconvert stationary and flying qubits.
2. The ability to faithfully transmit flying qubits between specified locations,

where flying qubits are the entities that carry quantum information over distance between, say, two quantum computer nodes.

The first five criteria still represent a useful context in which to appraise the viability of a proposed pathway to quantum computer development. They also provide a set of goals that scientists must strive to achieve if they are going to have any chance of success. Hence, in this paper, we review progress toward development of a donor-based quantum computer in silicon from this convenient standpoint.

Interest in impurity-based quantum computing in silicon grew quickly after an architecture for a quantum computer based on encoding information on the donor nuclei of individual phosphorus atoms embedded in a silicon matrix was proposed by Kane in 1998.³⁷

The importance of being able to initialize and readout qubits prompted research into the development of electron reservoirs that could be manipulated via a suitable array of gates to allow electrons to be loaded onto or removed from a nearby qubit in a precisely controlled manner. Advances in single electron manipulation and spin readout have relied on this key breakthrough.^{15,16,38–40}

A. Phosphorus donor qubits

Figure 1(a) shows a scanning electron microscope (SEM) image of a phosphorus spin qubit device.³⁹ Under appropriate electrostatic conditions, resonant tunneling of an electron can occur between a phosphorus donor and the island of a gate-defined quantum dot structure or silicon single electron transistor (Si SET) nearby. The Si SET is formed using Al gates deposited on a high-quality 5 nm SiO₂ thermal oxide grown on a high-purity Si substrate.⁴¹ A small reservoir of electrons is formed on the SET island through appropriate choices of top-gate (V_{TG}) and barrier-gate (V_{LB} , V_{RB}) potentials. Prior to gate formation, a small number of P atoms were implanted at low energy (14 keV) through the gate oxide into the $90 \times 90 \text{ nm}^2$ region indicated by the dashed boundary, and then the sample was subjected to a rapid thermal anneal to repair the implant damage and activate the dopants.³⁹ The ion fluence was chosen to maximize the likelihood that three donors would be located at a distance of $\sim 30\text{--}60 \text{ nm}$ from the SET island and could be tunnel-coupled to it. Similar results have been obtained for a number of devices, and in each case, the number of

charge transitions observed is compatible with the number of donors expected to be found within the appropriate tunneling distance from the SET island for the given P implant fluence.⁴²

Figure 1(b) shows a schematic of the relationship between the energy levels of the donor ground state and the Fermi level of the SET island under resonance conditions for electron transfer. In the presence of a magnetic field, the ground state is spin-split, and the electrostatic landscape can be tuned so that the spin-up state can tunnel to the SET island while the spin-down state is blocked. This resonant tunneling condition is achieved using appropriate tuning of the plunger gate (V_{PL}) voltage. Transfer of an electron from the charge center to the island has a dramatic effect on the source-drain current, so the tunneling event can readily be detected. Figure 1(c) shows a typical charge stability diagram for one of these devices. The breaks are due to charge transfer events. Since the tunneling probability is very sensitive to the distance between the charge centers and the island, different regions of the bias-spectroscopy diagram correspond to tunneling events from different charge centers. In this particular case, transitions arising from electron tunneling between P donors and the SET island are observed for $\sim -1.5 \text{ V} < V_{PL} \leq -0.7 \text{ V}$, while other charge transfer events most likely associated with shallow traps are observed for plunger gate voltages in the range $\sim -0.7 \text{ V} < V_{PL} < 0 \text{ V}$.³⁹ The microwave line shown in Fig. 1(a) is used to produce an oscillating magnetic field perpendicular to the surface of the device that can be used to manipulate the spin state of the P electron.¹⁵ The spin of the P nucleus can also be read out via the hyperfine interaction arising from the overlap between the wave-functions of the electron and the ³¹P nucleus.¹⁶ Further details of the control and readout of P-donor qubits are described later in this section and clearly illustrate that the P-donor qubit devices satisfy the DiVincenzo criterion of having well-characterized qubits. The scalability requirement will be addressed in Sec. IV.

Mohiyaddin *et al.*⁴³ have used a spatial metrology method to determine the locus of points that is compatible with the measured characteristics of a particular donor transition in a device similar to that in Fig. 1(a). The triangulation method finds the intersection of three loci of points consistent with electrostatics modeling of the ground state energy of the donor-bound electron, quantum-mechanical tight binding modeling of the donor-bound electron wave-function to match the Stark-shift of the hyperfine coupling, and geometric capacitance modeling to match the measured capacitive coupling between the donor and the surrounding electrodes. From a device fabrication point of view perhaps, the most interesting result of this metrology study is not the locus of points that is consistent with the location of a particular donor for a particular set of measurement conditions, but instead it is the limitations that can be determined for the accuracy of donor placement required to obtain a measurable tunneling transition. The two key factors involved are that a sufficient change in the position of Coulomb peaks of the Si SET must occur when the electron tunnels from the donor to the island and that the tunnel rates need to be in the range of $\sim 10 \mu\text{s}$ – 100 ms to be experimentally detectable. This second condition places the greatest restriction on the tolerance of the donor position, allowing donors within a band $\sim 5\text{--}6 \text{ nm}$ wide at an appropriate distance from the SET island to be utilized for the conditions described in the paper. Due to the exponential dependence of the tunneling rate on gate voltage, it is expected that this tolerance in donor position can be extended to a

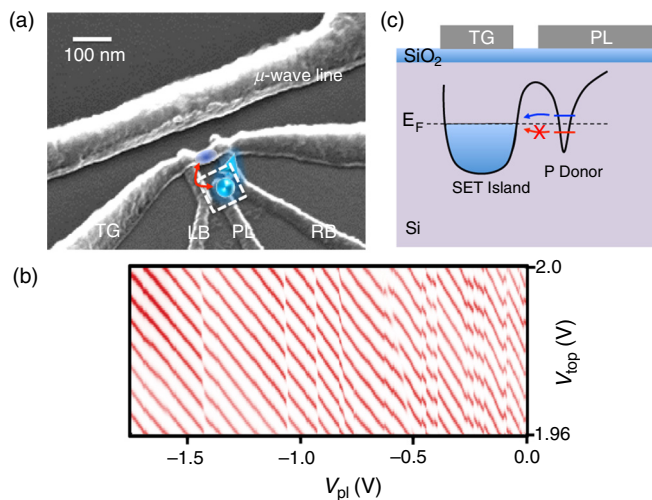


FIG. 1. Phosphorus spin qubit device structure and associated charge transitions. (a) Scanning electron micrograph of a typical device structure showing the top gate (TG) and left and right barrier gates (LB and RB, respectively) of the silicon SET (after Ref. 39). The region within the dashed boundary represents the area into which a small number of P atoms were implanted at low energy prior to gate formation. P donor electron spin readout is achieved via electron transfer between the donor and the SET island. The microwave strip line allows P electron spin manipulation. (b) Schematic of the relationship between the energy levels of the donor ground state and the Fermi level of the SET island under the resonance condition for electron transfer. (c) Typical charge stability diagram showing transitions arising from electron tunneling between the donor and the SET island ($V_{PL} \leq 0.7 \text{ V}$) in addition to other charge transfer events ($V_{PL} \geq 0.7 \text{ V}$) associated with shallow traps. Adapted with permission from Morello *et al.*, *Nature* **467**, 687 (2010). Copyright 2010 Springer.

band $\sim 10\text{--}12\text{ nm}$ wide. This tolerance in individual qubit placement with respect to gates is achievable using ion implantation as discussed in Sec. III, and, while qubit–qubit coupling via conventional exchange-coupling requires tolerances on qubit placement that are extremely stringent^{44–47} and not readily achievable using ion implantation, the flip-flop qubit presented in Sec. IV has greatly relaxed requirements for donor placement and provides a suitable pathway for pursuit of scale-up utilizing ion implantation.

B. P-donor qubits: Electron spin initialization and control

Initialization and control of P-donor spin qubits in Si was first demonstrated for the ^{31}P electron spin¹⁵ and for the ^{31}P nuclear spin¹⁶ in natural Si where the presence of the ^{29}Si atoms was a significant source of decoherence. These experiments were quickly followed by similar measurements on a ^{28}Si epilayer containing phosphorus spin qubit devices, which clearly demonstrated one of the key attributes of Si as a host for qubits, namely, that isotopically pure ^{28}Si epi-layers offer attractively long coherence times for donor qubits.⁴⁸

The electron spin initialization, readout, and control protocols for P-donor qubits are illustrated in Fig. 2. The SEM micrograph, Fig. 2(a), is the same as that in Fig. 1 but has been annotated to schematically depict the in-plane external magnetic field B_0 used to split the energies of the spin-up and spin-down states of the P-donor electron and the oscillating magnetic field, B_1 , produced by the microwave line (upper portion of the micrograph) and used to rotate the electron spin. Readout of the electron spin state is achieved through a process termed spin-to-charge conversion^{39,49} and involves spin-dependent tunneling of the electron from the P-donor to the SET island (lower portion of the micrograph). The shift in electrochemical potential arising from tunneling of the electron onto the SET island is large enough to switch the current from zero to its maximum value. Spin-dependent transfer to the SET island is achieved by applying a sufficiently large external magnetic field, B_0 , that the Zeeman splitting of the spin-up and spin-down states of the donor electron is larger than the thermal and electromagnetic broadening of the electron states of the SET island. This is typically achieved with magnetic fields, $B_0 \geq 1\text{ T}$, and with devices cooled to produce electron temperatures, $T_{\text{el}} \sim 200\text{ mK}$, and allows single-shot readout of the spin state of the electron.¹⁵

The qubit is first initialized in the $|\downarrow\rangle$ state through spin-dependent loading using appropriate biasing to satisfy the condition $\mu_{\downarrow} < \mu_{\text{SET}} < \mu_{\uparrow}$, Fig. 2(b). Then the electron spin states are plunged well below the SET island Fermi level, i.e., so that $\mu_{\downarrow}, \mu_{\uparrow} \ll \mu_{\text{SET}}$, while microwaves are applied to the transmission line to perform electron spin resonance (ESR), Fig. 2(c). The spin is then read out electrically via spin-to-charge conversion, Fig. 2(b), producing a pulse in the SET current if the electron was $|\uparrow\rangle$ and leaving the qubit initialized $|\downarrow\rangle$ for the next cycle.

Rabi oscillation measurements were performed on the electron spin state by applying single microwave pulses of varying duration, t_p , Fig. 2(e) and then reading out the spin-state. Due to hyperfine coupling between the P-donor electron and nuclear spins, Fig. 2(d), for each cyclic pulse sequence, a pulse with a microwave frequency ν_{e1} was immediately followed by one with frequency ν_{e2} . Since the nuclear spin can flip several times during the data acquisition, it was necessary to pulse on both nuclear-spin-up and nuclear-spin-down electron spin

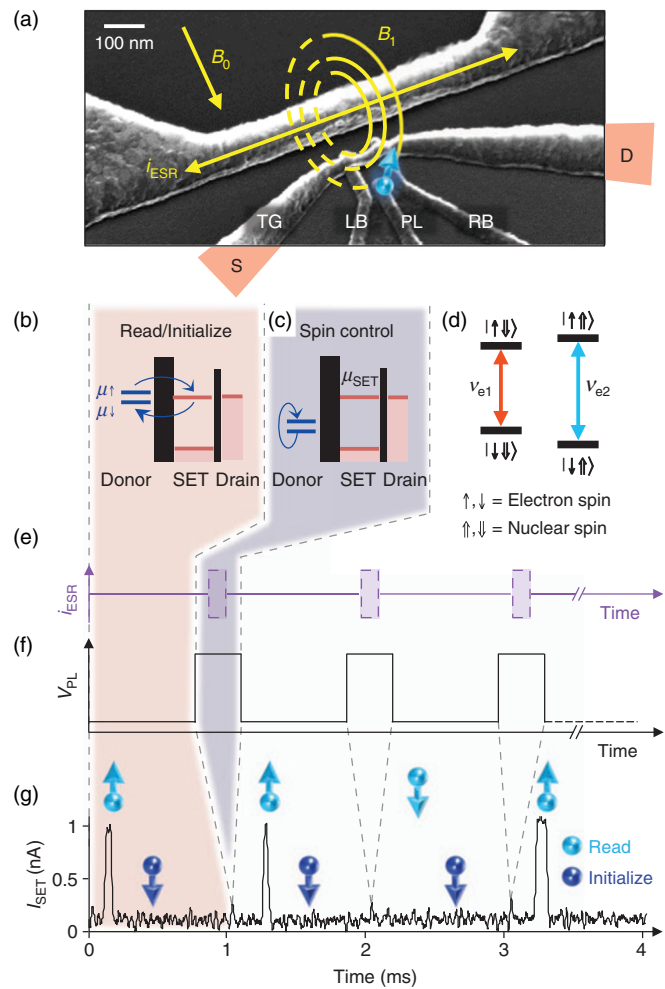


FIG. 2. P-donor qubit initialization, readout, and control scheme: (a) Scanning electron micrograph of a P-donor qubit device similar to the one used in the experiment described here. The SET configuration is the same as that in Fig. 1. The microwave transmission line is shown in the upper left portion. The donor (blue) is subject to an oscillating magnetic field B_1 from the transmission line, which is perpendicular to the in-plane external field B_0 . (b) Electron spin read/initialize: $\mu_{\downarrow} < \mu_{\text{SET}} < \mu_{\uparrow}$: a spin-up electron will tunnel from the donor to the SET island, to be later replaced by a spin-down electron, causing a pulse of current through the SET. A spin-down electron remains trapped on the donor throughout the phase. (c) Spin control: $\mu_{\downarrow}, \mu_{\uparrow} \ll \mu_{\text{SET}}$: electron spin states are plunged well below the SET island Fermi level, while microwaves are applied to the transmission line to perform electron spin resonance. (d) Energy level diagram of the ^{31}P electron–nuclear system. (e) Microwave pulse sequence and (f) synchronized plunger gate voltage waveform for performing and detecting spin manipulations (not drawn to scale). An arbitrary electron spin resonance pulse sequence is represented by each of the dashed purple boxes in panel (e). (g) An example of the I_{SET} response to four consecutive read/control events where a single microwave pulse of duration t_p is applied, taken at $B_0 = 1.07\text{ T}$. The pulse duration t_p has been set to give a high probability of flipping the electron spin. The duration of the pulses in I_{SET} gives the electron spin-down tunnel-in time (about 33 ms), while their delay from the beginning of the read phase gives the spin-up tunnel-out time (about 295 ms). Reproduced with permission from Pla *et al.*, Nature **489**, 541 (2012). Copyright 2012 Springer.

resonance (ESR) transitions. Figure 2(g) shows an example of the I_{SET} response to four consecutive read/control events, where a single microwave pulse of duration t_p is applied with an external magnetic field $B_0 = 1.07$ T. In collecting Rabi oscillation data, the pulse cycle was repeated 20 000 times for each t_p . The largest Rabi frequency achieved was 3.3 MHz for $B_1 \approx 0.12$ mT, corresponding to a $\pi/2$ rotation in about 75 ns. A $\pi/2$ rotation rotates a $|\uparrow\rangle$ or $|\downarrow\rangle$ state into the x - y plane on the Bloch sphere.⁵⁰ For descriptions of some of the most common pulsing techniques used in spin manipulation and control, see, for example, Bowman,⁵¹ Hahn,⁵² Rabi,⁵³ and Ramsey.⁵⁴

Hahn echo measurements yielded a transverse relaxation time, $T_2 = (206 \pm 12) \mu\text{s}$ for the P-donor electron spin, which is close to the value of 300 μs measured in natural Si samples,⁵⁵ indicating that the presence of the SET and the proximity of the Si/SiO₂ interface have little, if any, effect on the electron spin coherence time. Pla *et al.* were also able to infer a pure dephasing time of $T_2^* = (55 \pm 5)$ ns (see Hu *et al.*⁵⁶ for a detailed discussion of the different coherence times of relevance in quantum computing) so that the coherence time, T_2 , is almost a factor of 2000 times longer than the pure dephasing time, T_2^* . Pla *et al.* also determined the fidelities of the donor electron spin qubit operations: measurement fidelity ($77 \pm 2\%$), initialization fidelity ($>90\%$), and control fidelity ($57 \pm 2\%$). These fidelities refer, for repeated operations, to the percentage of operations for which the desired output state is achieved. In these experiments, the qubit control fidelity was adversely affected by random field fluctuations from the ²⁹Si nuclear spins present in the sample. In addition, Pla *et al.* noted that improvements in electronic filtering would lower the electron temperature, hence reducing the read/load errors and allowing fidelities $>90\%$ to be projected. As already noted and discussed later in this section, by removing the ²⁹Si, the use of ²⁸Si epi-layers exceptionally long coherence times can be obtained, and combining this device architecture with ²⁸Si yields a very good qubit.

C. P-donor qubits: Nuclear spin initialization and control

The qubit discussed above is also amenable to readout and control of the nuclear spin of the P-donor.¹⁶ The nuclear spin of the donor is very attractive for quantum computing applications because it represents a quantum state that is comparatively well-isolated from environmental sources of decoherence, and this was part of the reason P-donors in Si for quantum computing were originally proposed by Kane.³⁷ Due to the hyperfine coupling of the electron and nuclear spins, the status of the nuclear spin can be determined via a spectroscopic measurement of the electron spin. Figures 3(a) and 3(b), adapted from Ref. 16, show energy-level diagrams for the neutral state, D^0 , and the ionized state, D^+ , of the ³¹P-donor, respectively. The electron spin resonance (NMR) transitions are shown in red, while the nuclear magnetic resonance (NMR) transitions are shown in blue. \uparrow and \downarrow refer to the electron spin up and spin down states, respectively, while $\uparrow\uparrow$ and $\downarrow\downarrow$ refer to the up and down states of the nuclear spin. (For a comprehensive review of NMR techniques for quantum control and computation please, see Vandersypen and Chuang.⁵⁷) For the ionized ³¹P donor, Fig. 3(b), there is a single NMR transition, shown in purple. The ESR spectra, Fig. 3(c), were obtained for an applied field, $B_0 = 1.77$ T, and show the electron spin-up fraction f_{\uparrow} as a function of microwave frequency. The top trace corresponds to a ν_{e1} ESR

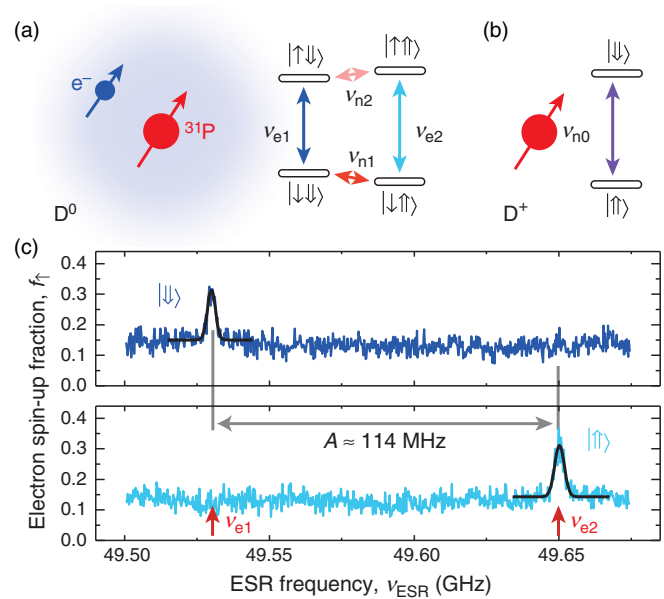


FIG. 3. Energy-level scheme and ESR spectra for readout of the nuclear spin state ³¹P-donor: (a) and (b) show energy-level diagrams for the neutral state, D^0 , and the ionized state, D^+ , of the ³¹P-donor, respectively. ESR transitions are shown in blue. Nuclear magnetic resonance (NMR) transitions are shown in red. \uparrow and \downarrow refer to the electron spin up and spin down states, respectively, while $\uparrow\uparrow$ and $\downarrow\downarrow$ refer to the up and down states of the nuclear spin. For the ionized ³¹P donor, (b), there is a single NMR transition, shown in purple. (c) ESR spectra for an applied field, $B_0 = 1.77$ T showing the electron spin-up fraction f_{\uparrow} as a function of microwave frequency: top trace corresponds to a ν_{e1} ESR transition (nuclear spin state $|\downarrow\downarrow\rangle$), bottom trace to an active ν_{e2} ESR transition (nuclear spin state $|\uparrow\uparrow\rangle$). Reproduced with permission from Pla *et al.*, Nature **496**, 334 (2013). Copyright 2013 Springer.

transition (nuclear spin state $|\downarrow\downarrow\rangle$) and the bottom trace to an active ν_{e2} ESR transition (nuclear spin state $|\uparrow\uparrow\rangle$).

By performing repeated measurements of the nuclear spin state, Pla *et al.* observed that it remained unchanged for several minutes before switching to the opposite state. The nuclear spin was also predominantly oriented in the $|\uparrow\uparrow\rangle$ state, and they attributed this to an electron–nuclear spin flip-flop process where the energy difference between the states $|\uparrow\downarrow\rangle$ and $|\downarrow\uparrow\rangle$, Fig. 3(a), is released to the phonon bath. In their experiments, $E_{\uparrow\downarrow} - E_{\downarrow\uparrow} \gg k_B T$, and hence this process acted only in the direction $|\uparrow\downarrow\rangle \rightarrow |\downarrow\uparrow\rangle$ so that only spontaneous emission of phonons occurred and phonon interactions were not responsible for the observed nuclear spin jumps in the opposite direction, i.e., from $|\uparrow\uparrow\rangle \rightarrow |\downarrow\downarrow\rangle$. Instead, this transition originated from the readout process, where the donor underwent repeated ionization and neutralization events.

In NMR experiments on the ³¹P-donor, for the neutral donor, D^0 , there are two NMR frequencies, ν_{n1} and ν_{n2} , while for the ionized donor, D^+ , there is only one, ν_{n0} , Figs. 3(a) and 3(b), respectively. The transition frequencies are given by $\nu_{n1} = A/2 + \gamma_n B_0$, electron spin $|\uparrow\rangle$, $\nu_{n1} = A/2 - \gamma_n B_0$, electron spin $|\downarrow\rangle$, and $\nu_{n0} = \gamma_n B_0$, where $A = 117.53$ MHz is the hyperfine coupling constant and $\gamma_n = 17.23$ MHz T⁻¹ is the nuclear gyromagnetic ratio.⁵⁸

Figure 4 shows Rabi oscillation data for a single ³¹P nuclear spin for both the neutral donor, (b), and ionized donor (e), states.¹⁶

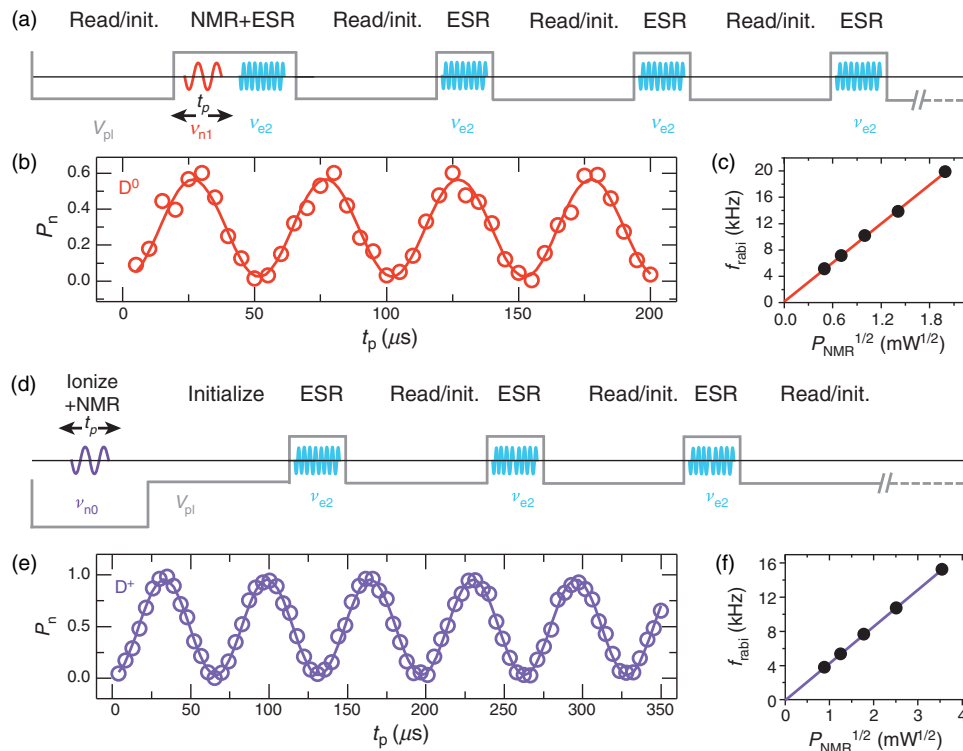


FIG. 4. Rabi oscillation data for a single ^{31}P nuclear spin for both the neutral donor, (b), and ionized donor (e), states. (a) The pulse sequence used for coherent rotation of the nuclear spin with the donor in the neutral, D^0 , state. Plunger gate voltage waveform is shown as a gray line and NMR and ESR pulses are shown in red and blue, respectively. (b) Rabi oscillation data for the nuclear spin of a neutral ^{31}P -donor with a magnetic field, $B_0 = 1.07\text{ T}$ and an applied radio frequency NMR power, $P_{\text{NMR}} = 4\text{ mW}$ and $\nu_{n1} = 75.726\text{ MHz}$. (c) Linear dependence of the Rabi frequency when plotted as a function of the square root of the applied NMR power or excitation amplitude. (d) Pulse sequence used to perform the Rabi oscillations on the nuclear spin of the ionized donor. (e) Rabi oscillation data for an ionized donor for $B_0 = 1.77\text{ T}$, $P_{\text{NMR}} = 126\text{ mW}$, and $\nu_{n0} = 30.5485\text{ MHz}$. (f) Linear dependence of the Rabi frequency on the excitation amplitude. Reproduced with permission from Pla *et al.*, *Nature* **496**, 334 (2013). Copyright 2013 Springer.

Figure 4(a) depicts the pulse sequence used for coherent rotation of the nuclear spin with the donor in the neutral, D^0 , state. The plunger gate voltage waveform is shown as a gray line, while the NMR and ESR pulses are shown in red and blue, respectively. In the experiment, after application of a coherent NMR pulse at ν_{n1} for duration, t_p , the nuclear spin state was read by probing the ν_{e2} ESR transition with 300 single-shot adiabatic inversion and electron-spin readout measurements, lasting approximately 300 ms, and a nuclear spin orientation was ascribed to the measurement by comparison of the electron-spin-up fraction $f_{\uparrow}(\nu_{e2})$ to a threshold. Figure 4(b) shows the Rabi oscillation data for the nuclear spin of a neutral ^{31}P -donor with a magnetic field, $B_0 = 1.07\text{ T}$, and an applied radiofrequency NMR power, $P_{\text{NMR}} = 4\text{ mW}$, and $\nu_{n1} = 75.726\text{ MHz}$. The pulse sequence of part (a) was repeated tens of times for each Rabi pulse length, t_p , with multiple sweeps of t_p to give a total of 200 measurements at each t_p . By recording the number of spin flips, the flip probability, P_n , could be determined for each value of t_p . The solid line is a fit to the data of the form $P_n = K \sin^2(\pi f_{\text{Rabi}} t_p)$, where K and f_{Rabi} are the fitting parameters. Figure 4(c) shows the linear dependence of the Rabi frequency when plotted as a function of the square root of the applied NMR power, i.e., the excitation amplitude.

In the case of the ionized donor, D^+ , a different pulse sequence was used to perform the Rabi oscillations as depicted in Fig. 4(d). The

electron was removed from the donor before applying a coherent NMR pulse. The electron was then replaced on the donor so that a single shot readout of the nuclear spin could be performed. Figure 4(e) shows Rabi oscillation data for an ionized donor for $B_0 = 1.77\text{ T}$, $P_{\text{NMR}} = 126\text{ mW}$, and $\nu_{n0} = 30.5485\text{ MHz}$, again with each measurement obtained from 200 measurements of the nuclear spin state. Figure 4(f) again shows the linear dependence of the Rabi frequency on the excitation amplitude.

It is interesting to compare the Rabi oscillation data for the neutral and ionized states of the donor, Figs. 4(b) and 4(e), respectively. For the neutral donor, the visibility of the oscillations is $\sim 60\%$, and this deviation from ideality is most likely due to incorrect initialization of the $|\uparrow\rangle$ state of the electron due to heating caused by the microwave pulse chain used in readout. For the ionized donor, near-unity visibility is obtained due to the fact that the electron has no influence on the nuclear spin state while the donor is ionized.

Pla *et al.* also performed Ramsey fringe measurements to find the dephasing times, T_2^* , for the nuclear spins of the neutral and ionized states of the donor and found that for the neutral donor, $T_2^*(\text{D}^0) = (3.3 \pm 0.3)\text{ ms}$. These dephasing times are $\sim 10^4$ times longer than the value measured for the electron spin (see discussion earlier in this section). Noting that many of the magnetic fluctuations that contribute to T_2^* occur on timescales that are much

longer than the typical nuclear spin manipulations time of $\sim 25 \mu\text{s}$ for a π -pulse, Pla *et al.* were able to use spin-echo techniques to reverse a significant portion of the dephasing to achieve transverse relaxation times of $T_2(D^0) = (3.5 \pm 0.1) \text{ ms}$ for the nuclear spin of the neutral donor and $T_2(D^+) = (60.0 \pm 0.9) \text{ ms}$ for the ionized donor.¹⁶ It was considered that ionizing the donor removed the connection between the nuclear spin precession frequency and sources of electrical noise so that the nuclear spin was better isolated from the environment giving rise to the longer coherence times.

Single-shot readout of the nuclear spin state of the ^{31}P -donor in these experiments is an example of quantum non-demolition (QND) measurement.⁵⁹ The quantum jumps of the nuclear spin occur through the interaction between the nuclear and electron spins and can be viewed as a deviation from QND ideality. Pla *et al.* were able to measure a lifetime for the $|\uparrow\rangle$ nuclear spin state of $T_{\uparrow} = (1500 \pm 360) \text{ s}$ and a shorter lifetime of $T_{\downarrow} = (65 \pm 15) \text{ s}$ for the $|\downarrow\rangle$ nuclear spin state. This shorter time was due to phonon modulation of the hyperfine coupling. Combining these lifetimes with the optimal measurement time of $T_{\text{meas}} = 104 \text{ ms}$ yielded QND fidelities of $F_{\text{QND}}(|\uparrow\rangle) = \exp(-T_{\text{meas}}/T_{\uparrow}) = 0.999\,93(2)$ and $F_{\text{QND}}(|\downarrow\rangle) = \exp(-T_{\text{meas}}/T_{\downarrow}) = 0.9984(4)$. At the time, these were the highest reported fidelities for any solid-state qubit and demonstrated that ^{31}P -donor nuclear spins could be used to form a quantum memory or a high-fidelity qubit, and the experiments certainly showed that the ^{31}P -donor qubits satisfy DiVincenzo criteria 2, 3, and 5: the ability to initialize the qubits to a simple fiducial state, long relevant decoherence times (which became even longer with the removal of the ^{29}Si from the vicinity of the donor qubits as is the next topic of discussion in this section), and a qubit-specific measurement capability.

D. P-donor qubits: Isotopically engineered ^{28}Si epilayers

Muhonen *et al.*⁴⁸ showed in 2014 that exceptionally long coherence times for electron and nuclear spin qubits in Si can be obtained by removal of the ^{29}Si atoms that are present in natural Si. An SEM micrograph of the device structure used in the experiments is shown in Fig. 5(a). While this device is similar to those previously discussed in this section, it differs slightly in terms of the gate layout to bring the microwave antenna into closer proximity to the P donors to improve the coupling. Also, between the microwave antenna and the SET, an extra pair of Al gates has been added to obtain additional control of the donor potential in relation to that of the SET. The biggest difference between this device structure and those discussed earlier is that the P-donor qubit was formed in a 900 nm thick ^{28}Si enriched layer grown by molecular beam epitaxy (MBE) on a natural silicon substrate. The ^{29}Si was depleted to 800 ppm in the ^{28}Si epi-layer. A schematic of the epi-layer structure is shown in Fig. 5(b). Rabi oscillations associated with operation of the device as an electron spin qubit are shown in Fig. 5(c) and continue for over 500 μs , which is a great improvement over the decay time of less than 1 μs that was measured in natural-Si. The ESR line was also extremely sharp, having a full-width at half-maximum (FWHM) of 1.8 kHz in one of the devices. It should also be noted that improvements in electronic filtering yielded an electron temperature $T_{\text{el}} \approx 100 \text{ mK}$ for these measurements, which is a factor of 2 lower than that in the earlier electron-spin measurement work of Pla *et al.*¹⁵ presented earlier in this section.

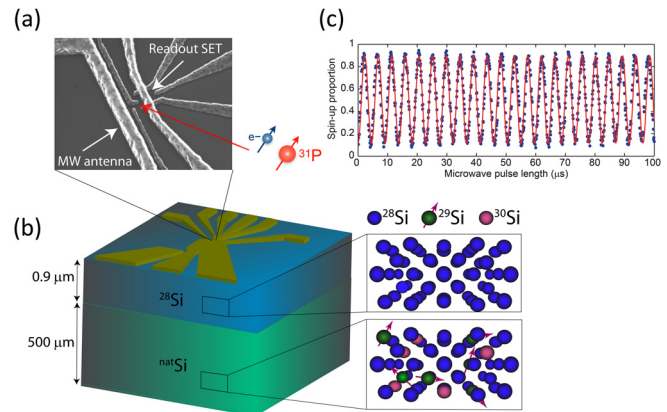


FIG. 5. Silicon-28 epi-layer P-donor spin qubit device structure and associated electron-spin Rabi oscillations. (a) Scanning electron micrograph of the device structure showing the microwave antenna (MW) and the readout SET. (b) Schematic of the ^{28}Si epi-layer structure on a natural-Si substrate. (c) Rabi oscillations of the electron-spin qubit. Adapted with permission from Muhonen *et al.*, Nat. Nanotechnol. **9**, 986 (2014). Copyright 2014 Springer.

Ramsey-fringe data for the ^{31}P -donor- ^{28}Si matrix qubit device yielded a pure dephasing time for the electron-spin of $(T_2^*)_{\text{e}} = 270 \mu\text{s}$, which is a 5000-fold improvement over the value of 55 ns obtained for the P-donor qubit in natural-Si.^{15,48} Hahn-echo measurements yielded a transverse relaxation time, $(T_2)_{\text{e}} \approx 1 \text{ ms}$, for the electron-spin, which is a factor of 5 greater than that in natural-Si. By employing Carr–Purcell–Meiboom–Gill (CPMG) dynamical decoupling sequences, Muhonen *et al.* were able to extend this to $(T_2^{\text{CPMG}})_{\text{e}} = 0.56 \text{ s}$. While these coherence times are significantly longer than those obtained in natural-Si they are still considerably shorter than the values of up to and exceeding 39 m that have been reported for bulk-ensemble measurements of ^{31}P -donors in ^{28}Si .

For the nuclear-spin of the ^{31}P -donor- ^{28}Si matrix qubit device, Muhonen *et al.* reported a dephasing time of $(T_2^*)_{\text{n}} \approx 500 \mu\text{s}$ for the neutral, $^{31}\text{P}^0$, state of the donor and $(T_2^*)_{\text{n}+} = 0.6 \text{ s}$ for the ionized, $^{31}\text{P}^+$, state. Hahn-echo measurements yielded a transverse relaxation time, $(T_2)_{\text{n}+} = 1.75 \text{ s}$, for the nuclear-spin of the ionized donor, and application of CPMG dynamical decoupling sequences extended this to $(T_2^{\text{CPMG}})_{\text{n}+} = 35.6 \text{ s}$. The electron-spin control fidelity was estimated to be $F_{\text{e}}^{\text{e}} \approx 99.6\%$, compared to the value of 57% found for natural-Si. For the nuclear-spin, $F_{\text{e}}^{\text{n}0} \approx 99.9\%$ for the neutral donor and $F_{\text{e}}^{\text{n}+} \approx 99.99\%$ for the ionized donor.

To investigate why the coherence times obtained in the P-donor ^{28}Si epi-layer devices, although very long compared to natural-Si devices, were still considerably shorter than the values obtained in bulk-ensemble measurements of ^{31}P -donors in ^{28}Si ,^{14,60,61} Muhonen *et al.* performed noise spectroscopy measurements on the P-donor devices and were able to conclude that it was likely that the electron spin coherence was limited by thermal and magnetic noise external to the device and not something intrinsic to the device itself and that the coherence times could therefore be further improved by employing engineering solutions to reduce the influence of external noise sources. One noise source that was identified was some instability of the external magnetic field B_0 produced by the superconducting solenoid.

By combining randomized benchmarking analysis protocols⁶² to reveal systematic errors that contribute to reductions in gate operation

fidelities with gate set tomography (GST) protocols⁶³ that helped reveal the sources of these errors, it was possible to achieve an average gate fidelity of 99.942(8)%, an improvement on the previous value of 99.90(2)%. The GST analysis showed that there was a 4.4% rotation error in some of the gate operations which having been identified could be removed. The GST analysis⁶³ also revealed the presence of non-Markovian or environmental noise⁶⁴ sources whose origins would require further investigation before greater gate fidelities could be achieved.

The ³¹P-donor:²⁸Si matrix qubit devices provided other examples of quantum control. For example, Freer *et al.*⁶⁵ demonstrated the transfer of the initial quantum state of the ³¹P-donor electron to the nuclear spin via electron–nuclear double resonance (ENDOR) techniques followed by storage of this state on the nuclear spin and then readout via transfer of the quantum-state back to the electron. Storage of the coherent state for times up to 80 ms could be achieved using dynamical decoupling pulses to maintain the nuclear spin state.

Another interesting application of these devices was to perform a demonstration of violation of the Bell/Clauser–Horne–Shimony–Holt (CHSH) inequality.^{66–68} Exploration of Bell’s inequality requires generation of Bell states, which are four specific maximally entangled quantum states of two qubits. For the ³¹P-donor device, these states are linear combinations of the spin-up and spin down states of the electron and nuclear-spin qubits: $|\psi^\pm\rangle = 1/\sqrt{2}(|\uparrow\downarrow\rangle \pm |\downarrow\uparrow\rangle)$ and $|\phi^\pm\rangle = 1/\sqrt{2}(|\uparrow\uparrow\rangle \pm |\downarrow\downarrow\rangle)$. To be able to perform the experiment, it was necessary to be able to initialize the two-spin system to a known state with high fidelity. For the ³¹P-donor:²⁸Si matrix qubit devices, the fidelity was limited by electron initialization errors, but by using selective initialization protocols, it was possible to obtain a two-spin initialization fidelity of 97%.⁶⁹

Measurement of the prepared entangled state required high-fidelity single-shot projective readout. In the measurements, readout of the electron spin-state was destructive because it involved spin-dependent tunneling from the donor to the SET island so that the electron was lost in the process. The nuclear spin-state, however, was measured through a quantum non-demolition (QND) process where the nuclear spin-state was mapped onto that of the electron, as discussed earlier in this section. The four-level energy diagram of the electron–nuclear spin system, Fig. 3(a), together with the set of resonant microwave and radiofrequency signals, ν_{e1} , ν_{e2} , ν_{n1} , and ν_{n2} , that were available to control the spin transitions allowed access to the full two-qubit Hilbert space. The QND readout allowed repetitive measurement of the nuclear spin-state to be performed without affecting the spin-state so that fidelities >99.9% could be attained. Any observable in the four-level system could be mapped to the nuclear spin to take advantage of the high-fidelity QND measurement.

The CHSH inequality violation protocol⁶⁸ is an experimentally realizable form of Bell’s inequality violation, and this was the protocol adapted by Dehollain *et al.* in their measurements. Further details of how the measurements were performed can be found in the paper,⁶⁶ but within the framework proposed by Bell and realizable via the CHSH protocol, for a physical system that exhibits locality [distant objects that have interacted in the past cannot instantaneously affect each other’s state (not so distant here but that is the general concept)] and realism (their properties exist before they are observed), measurement of a parameter called the Bell parameter, S , will yield $|S| \leq 2$, Bell’s inequality, while quantum mechanics predicts $S_{\max} = 2\sqrt{2}$ for a

maximally entangled state. In their work, Dehollain *et al.* found $S = 2.70 \pm 9$ in clear violation of Bell’s inequality and local-reality theories while adding further confirmation that entangled quantum states have no classical counterpart.

E. P-donor qubits: Stark-tuning

A very important contribution to progress in donor-based quantum computing in Si and realization of possible pathways to scale-up was the Stark-tuning work of Laucht *et al.*⁷⁰ The work showed that a concept that was originally proposed in the Kane paper³⁷ could be used to tune the donor into resonance with the applied microwave field by Stark-shifting of the donor energies through application of an electric-field via an electrostatic gate, called an “A-gate.”

The concept is illustrated in Fig. 6. Part (a) of the figure shows an SEM micrograph of a device similar to the one used in the experiment. Again, it is a ³¹P-donor:²⁸Si matrix qubit device similar to that in Fig. 5 but with an extra set of gate electrodes. These gates, the Donor Fast, DF, and Donor Slow, DS, gates and the Top Gate AC (TGAC), are used to tune the potential and the electric field at the location of the P-donor. The SET is shown in the top right of the figure, while the microwave antenna is shown in the bottom left. Figure 6(b) schematically illustrates the distortion of the electron wave-function of the donor upon application of an electrostatic potential to an electrode, the “A-gate.” With an applied bias, the electron wave-function is distorted away from the nucleus causing Stark-shifting of the energy levels of the donor electron–nucleus system, Fig. 6(c). Gate-controlled distortion of the electron wave-function modifies the electron–nuclear hyperfine coupling, A , and the electron gyromagnetic ratio, γ_e , shifting the ESR, ν_{e1} and ν_{e2} , and the NMR, ν_{n1} and ν_{n2} , transition frequencies.

This experiment demonstrated that individual donors could be tuned in and out of resonance with the frequency of a single continuous-wave microwave source, and this greatly simplifies the infrastructure required for scale-up and reduces the costs. Randomized benchmarking measurements to quantify the average gate fidelities that could be obtained using this electrically controlled qubit manipulation method yielded fidelities in excess of 99% for both the electron and the nuclear spins, which were similar to those obtained from pulsed ESR/NMR randomized benchmarking protocols.⁷⁰

F. P-donor qubits: Dressed states

The same ³¹P-donor:²⁸Si matrix qubit device structure as that presented in Fig. 6(a) was also used to explore a quite different qubit system: the dressed spin qubit in Si.⁷¹ Here, production of a dressed quantum state involved the use of the microwave (MW) driving field, B_1 , to coherently interact with the donor electron spin so that the resulting eigenstates of the driven system are the entangled states of the photons of the driving field and the electron spin system. The eigenstates of the system are no longer the spin-up and spin-down states of the electron-spin, but are the symmetric and antisymmetric superpositions of these states with the driving field. The relevant energy-level diagram is illustrated in Fig. 7. N is the total number of excitations in the system, while n is the number of resonant photons in the driving field, which in turn depends on the power of the MW drive field.

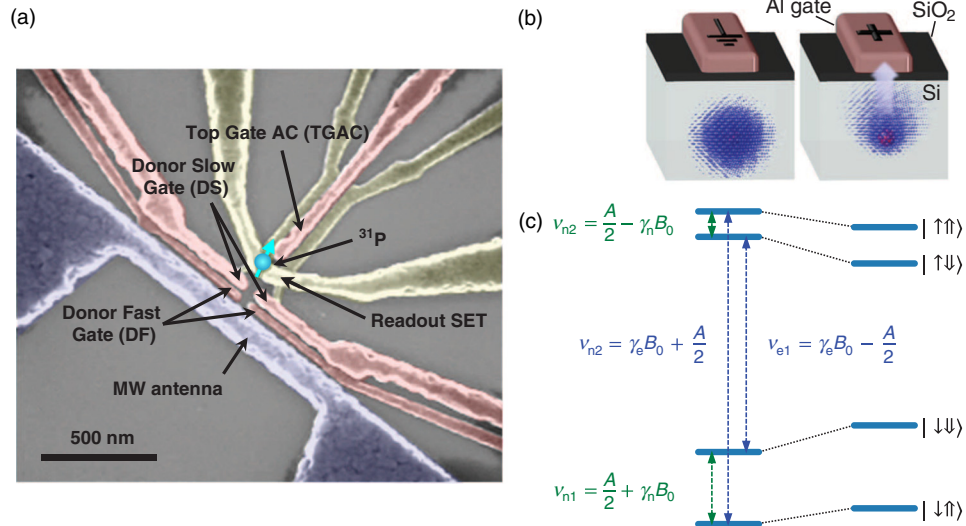


FIG. 6. Use of an electrostatic A-gate to Stark-shift the energy levels of the P-donor into resonance with an applied microwave field: (a) SEM micrograph of the ^{31}P -donor: ^{28}Si matrix qubit device structure used in the experiment, showing the microwave antenna (MW) (lower left) and the readout SET (upper right) and the gates: Donor Fast (DF), Donor Slow (DS), and Top Gate AC (TGAC) that are used to tune the potential and electric field at the location of the donor. The aerial location of the ^{31}P -donor with respect to the island of the SET is illustrated schematically. (b) Schematic illustration of the distortion of the electron wave-function of the donor upon application of an electrostatic potential to the A-gate: (left) with no applied bias, and (right) with a Stark-shifting bias applied. (c) Energy level diagram of the neutral ^{31}P -donor: Gate-controlled distortion of the electron wave-function modifies the electron-nuclear hyperfine coupling, A , and the electron gyromagnetic ratio, γ_e , shifting the ESR, ν_{e1} and ν_{e2} , and the NMR, ν_{n1} and ν_{n2} , transition frequencies. Reproduced with permission from Laucht *et al.*, *Sci. Adv.* **1**, e1500022 (2015). Copyright 2017 Author(s), licensed under a Creative Commons Attribution 4.0 License.

The resulting spectra for different microwave powers are shown in Fig. 8. To obtain the spectra, a strong resonant driving field P_{pump} was applied to dress the spin state, while a weaker probe field $P_{\text{probe}} = P_{\text{pump}} - 26 \text{ dB}$ was scanned in frequency to record the triplets (named Mollow triplets).⁷² The spectra represent the spin-up probability after application of the MW pulses. The colored lines match the

transitions in the energy-level diagram, Fig. 7. The insets on the left show Rabi measurements for the same MW powers. Laucht *et al.* also demonstrated four different methods of dressed qubit control and measured favorable qubit lifetimes ($\sim 1 \text{ s}$) and coherence times ($\sim 1\text{--}20 \text{ ms}$) showing the potential of dressed spin qubits for applications in quantum-information processing.

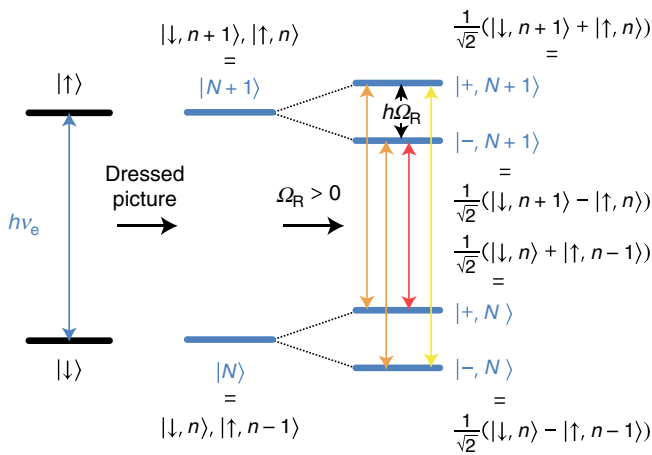


FIG. 7. Energy-level diagram of the P-donor electron-spin in the spin picture (left) and the dressed qubit picture (right). In the dressed state, the energy level splitting is given by $\hbar\Omega_{\text{Rabi}}$ where Ω_{Rabi} is the electron Rabi frequency, which in turn is proportional to the microwave excitation amplitude, i.e., $P_{\text{ESR}}^{1/2}$. Reproduced with permission from Laucht *et al.*, *Nat. Nanotechnol.* **12**, 61 (2017). Copyright 2017 Springer.

G. P-donor qubits: Coupled qubits

Having established suitable single qubits, another essential step in developing a viable quantum computing platform is to demonstrate two-qubit coupling and controlled two-qubit gate operations.⁷³ In an early demonstration of qubit-qubit coupling in P:Si, Dehollain *et al.*⁶⁹ observed readout events in a P ion implanted device in natural-Si that were consistent with two strongly exchange coupled ^{31}P electron-spins. Evidently the stochastic nature of the ion implantation process had fortuitously placed two P atoms in appropriate positions for strong coupling to occur. However, due to the strength of the coupling and the fact that this was an early generation of devices, the extra gates that might have enable more detailed control and spectroscopic analysis of the coupled qubits were not available, and the presence of the ^{29}Si nuclear-spins was a compounding issue.

Pla *et al.*⁷⁴ also reported experimental demonstration of single-shot readout, coherent control, and measurement of the coherence properties of an individual ^{29}Si nuclear-spin in natural-Si coupled to a ^{31}P -donor. They demonstrated the ability to coherently manipulate the ^{29}Si nuclear-spin coupled to both the neutral, D^0 , and ionized, D^+ , states of the P-donor and measured a transverse relaxation time, $T_2 = (6.3 \pm 0.7) \text{ ms}$, for the ^{29}Si coupled to the ionized donor, in

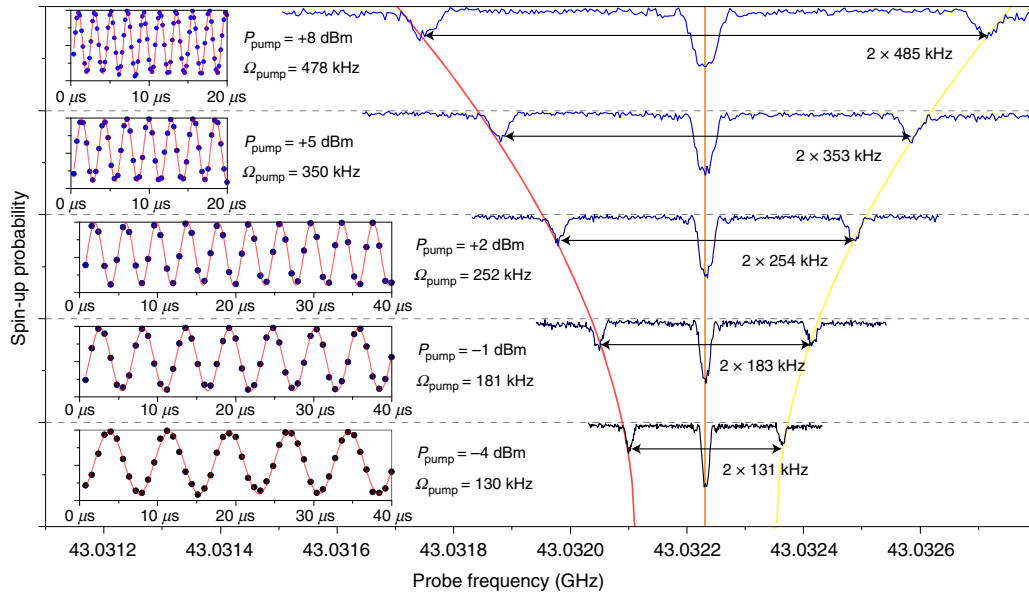


FIG. 8. Spectra of the dressed electron spin qubit for different MW powers. The spectra represent the spin-up probability after application of the MW pulses. To obtain the spectra, a strong resonant driving field P_{pump} was applied to dress the spin state while a weaker probe field $P_{\text{probe}} = P_{\text{pump}} - 26$ dB was scanned in frequency to record the triplets (Mollow triplets). (The curves are shifted in frequency to compensate for a slight drift in the background magnetic field B_0). The insets on the left show Rabi measurements for the same MW powers (vertical scale is electron spin-up probability with range 0–1) and with Rabi frequencies that match the splitting between the peaks of the Mollow triplets. Reproduced with permission from Laucht *et al.*, Nat. Nanotechnol. **12**, 61 (2017). Copyright 2017 Springer.

good agreement with bulk measurements. Understandably, when ^{28}Si epi-layers became available, focus quickly shifted away from $^{31}\text{P} - ^{29}\text{Si}$ coupled qubits.

More recently, conditional quantum operation has been demonstrated for a pair of exchange coupled single P-donor spin qubits in an ion implanted ^{28}Si epi-layer device, as illustrated in Fig. 9.¹⁷ In this device, as in previous devices, ion implantation was performed through a lithographically defined window. Here, the implantation fluence was increased so that there was a reasonable likelihood of finding two donors that were close enough to be exchange coupled but not so close that the exchange coupling would be too strong. These fortuitously placed donor pairs were then discovered by looking for suitable regions in the charge stability diagram for the device. This is illustrated in Figs. 9(b) and 9(c).

Figure 9(a) shows an SEM micrograph of a device of the same type as that used in the study. The approximate location of the two exchange-coupled donors with respect to the gates and SET, based on the ion implantation window, is shown schematically. Part (b) of the figure shows a region of the charge stability diagram (i.e., SET current vs SET and donor gate voltages) for the implanted device. The implantation parameters were 10 keV P^+ ions implanted to a fluence of $1.25 \times 10^{12} \text{ cm}^{-2}$. The arrow indicates a region where the charge transitions of two different donors cross each other. Part (c) of the figure explores this region in more detail and shows the charge stability diagram for the two donor charge transitions obtained by scanning the voltages on the pulsing SET and the pulsing donor gates [in contrast to part (b), where the DC gates were scanned, a process that is associated with stronger capacitive coupling to the donors]. As noted by the authors, controlling the two pulsing gates above the donor

implantation area allows selective and independent control of the charge state of each donor, which can be set to either the neutral, D^0 (electron number, $N=1$), or the ionized, D^+ ($N=0$) state. Of particular importance is the fact that the electrochemical potential of the donors with respect to each other can be freely chosen so that the donor that ionizes first can be selected while the other remains neutral.

The Hamiltonian for the two weakly exchange coupled ^{31}P donors is given by¹⁷

$$H = (\mu_B/h)B_0(g_t S_{zt} + g_c S_{zc}) + \gamma_n B_0(I_{zt} + I_{zc}) + A_t \mathbf{S}_t \cdot \mathbf{I}_t + A_c \mathbf{S}_c \cdot \mathbf{I}_c + J(\mathbf{S}_t \cdot \mathbf{S}_c), \quad (1)$$

where B_0 is the static magnetic field value (1.4 T in this experiment), and the donor spins are described by the electron ($\mathbf{S}_t, \mathbf{S}_c$ with basis states $|\uparrow\rangle, |\downarrow\rangle$) and nuclear ($\mathbf{I}_t, \mathbf{I}_c$ with basis states $|\uparrow\rangle, |\downarrow\rangle$) spin 1/2 vector Pauli operators, with one donor spin being the control, “c,” qubit and the other being the target, “t,” qubit in a conditional quantum logic operation. μ_B is the Bohr magneton, h is Planck’s constant, and $g_t, g_c (\approx 1.9985)$ are the Landé factors $\Rightarrow g\mu_B/h \approx 27.97 \text{ GHz/T}$. $\gamma_n \approx -17.23 \text{ GHz/T}$ is the gyromagnetic ratio, and A_t, A_c are the electron–nuclear contact hyperfine interactions in the target and control qubits, respectively. J represents the exchange coupling strength. For the donor pair presented in the paper, the exchange coupling strength was spectroscopically measured to be $J = (32.06 \pm 0.06) \text{ MHz}$ and was weaker than the electron–nuclear hyperfine coupling, $A \approx 90 \text{ MHz}$, but greater than the resonance linewidth ($\sim 10 \text{ kHz}$) in the device, allowing a native two-qubit controlled-rotation gate to be obtained via a simple electron spin resonance pulse. Native here refers to the set of gate operations that can be

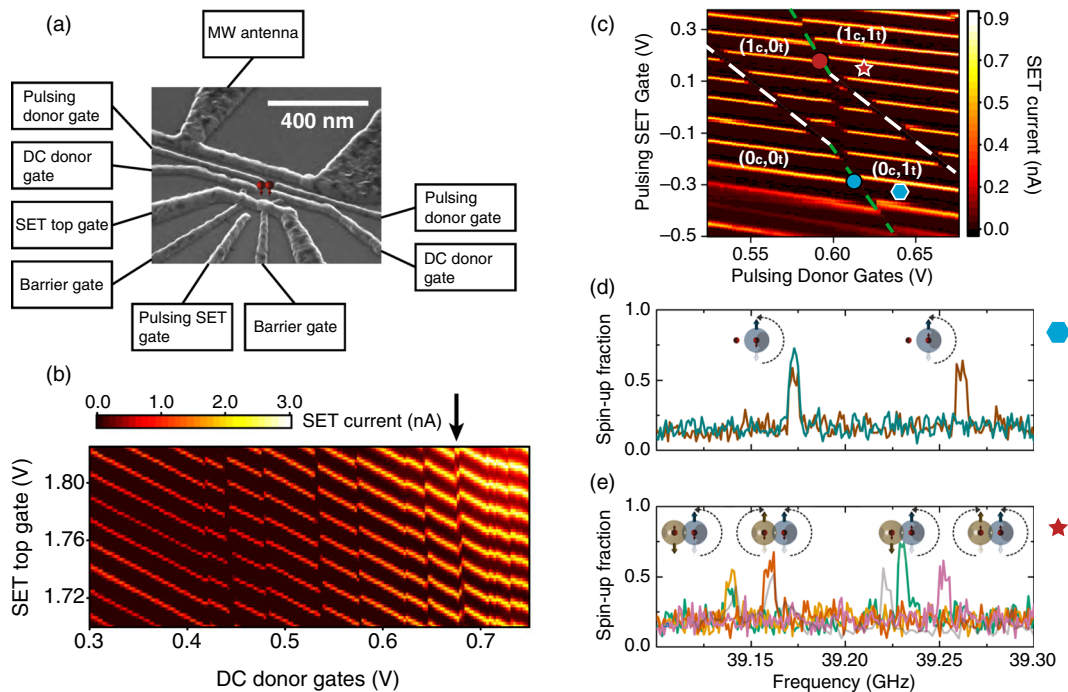


FIG. 9. (a) Scanning electron micrograph of a device of the type used in the experimental demonstration of two-qubit logic gate operation of a pair of weakly exchange coupled P-donors in a ^{28}Si device. The approximate location of the two exchange-coupled donors with respect to the gates and SET, based on the ion implantation window, is shown schematically. (b) Charge stability diagram (i.e., SET current vs SET and donor gate voltages) in a device implanted with 10 keV P^+ ions to a moderate fluence of $1.25 \times 10^{12} \text{ cm}^{-2}$. The arrow indicates a region where the charge transitions of two different donors cross each other. This region is explored in more detail in part (c), which shows the charge stability diagram for the two donor charge transitions obtained by scanning the voltages on the pulsing SET and the pulsing donor gates [unlike part (b), where the DC gates were scanned, which is associated with stronger capacitive coupling to the donors]. A two-electron honeycomb diagram is clearly seen. The dashed white lines indicate transitions of the control donor, while the dashed green lines indicate transitions of the target donor (see the text for description of control and target donors). The measurement demonstrates an access to all charge occupation regions. Blue and red circles identify the spin readout points for the target electron, while the blue hexagon and red star identify the spin control regions for different charge occupations. (d) An ESR spectrum acquired in the $(0_c, 1_t)$ region (blue hexagon), where the control donor is ionized. Only two ESR peaks arise, related to the nuclear spin configuration of the target donor. (e) ESR spectra of the target donor measured in the $(1_c, 1_t)$ region (red star) where the exchange coupling with the control electron gives rise to four main peaks corresponding to the four possible nuclear spin configurations, while the electron is in the $|\downarrow\rangle$ state. Adapted with permission from Mądzik *et al.*, Nat. Commun. **12**, 181 (2021). Copyright 2017 Author(s), licensed under a Creative Commons Attribution (CC BY) License.

performed directly on the particular quantum device/architecture and that can be combined to access other non-native operations to yield a universal gate set.

Returning to the charge stability diagram of Fig. 9(c), the four regions correspond to the possible configurations of the neutral, $N=1$, and ionized, $N=0$, charge states of the control, “c,” and target, “t,” qubits are identified together with the transition boundaries. The dashed white lines follow the control donor transition, while the dashed green lines follow the target donor. At the boundary between the $(0_c, 0_t) \leftrightarrow (0_c, 1_t)$ regions, for example, the target donor can be readout via spin-dependent tunneling to the SET island while the control donor remains ionized, and, in particular, the nuclear spin state of the target donor can be measured. This is illustrated by the ESR spectrum in Fig. 9(d), which shows the two ESR peaks consistent with the two possible nuclear spin orientations of the target ^{31}P donor. While the ESR trace for a single ^{31}P donor will usually only show one peak occasionally, the nuclear spin will flip during the scan, yielding two peaks.

If instead the qubit is operated near the $(1_c, 0_t) \leftrightarrow (1_c, 1_t)$ boundary where the target donor is read out but the control donor is

now in the neutral D^0 state, with the electron bound to it, repeated measurements of the ESR spectrum now yield four possible ESR peaks, Fig. 9(e), consistent with the exchange interaction J between the two-donor electrons. The four ESR peaks correspond to the four possible orientations of the two donor nuclear spins, while the control donor is in the $|\downarrow\rangle$ state. Having demonstrated spectroscopic measurement consistent with exchange coupled ^{31}P donors, the authors of the paper then demonstrated conditional and unconditional coherent control of the target qubit in the presence of the exchange-coupled control qubit, and, in particular, they demonstrated a hyperfine-controlled rotation (CROT) gate for the donor electrons, further details of which are discussed in Sec. IV B and can also be found in the paper.¹⁷

Following on from this work, Mądzik *et al.*⁷⁵ have completed a more detailed study of the quantum operations that can be achieved with this coupled qubit system by performing gate set tomography measurements. The measurements were performed on a three qubit processor formed from the two P-donor nuclei and one shared electron. A geometric two-qubit controlled-Z (CZ) gate was implemented in the study. The measurements demonstrated one-qubit gate fidelities up to 99.93(3)%, two-qubit gate fidelity of 99.21(14)%, and two-qubit

preparation/measurement fidelities of 98.95(4)%. As noted by the authors, these three metrics indicate that nuclear spins in silicon are approaching the performance demanded in fault-tolerant quantum processors. This provides further motivation for research into donor placement and coupling methods beyond the random donor placement, and hence somewhat fortuitous exchange coupling is achieved in this current work.

H. Donors other than phosphorus

Electron spin readout has also been demonstrated in a self-aligned device structure in natural-Si implanted with a small number of Sb donors.⁴⁰ In this device, polysilicon gates were used to form an SET at the SiO₂/Si interface as illustrated in Figs. 10(a) and 10(b). Using polysilicon gates for the SET allows the Sb donors to be implanted and activated after the SET gates are formed so that the donor positions are self-aligned with respect to the SET. This CMOS-compatible processing pathway can be advantageous for ion implantation approaches to qubit formation. Sb donors also offer low straggle during ion implantation and comparatively low diffusivity during the activation anneal, which can be advantageous for controlling donor placement with respect to surface gates and other structures. They also offer extra spin degrees of freedom.

Figure 11(a) shows an SEM micrograph of another Sb-qubit device.⁷⁶ In this case, it is a ¹²³Sb-donor:²⁸Si matrix qubit device in which the stable ¹²³Sb-isotope with the higher, $I = 7/2$, nuclear spin has been selectively ion implanted. The device structure is similar to that of Fig. 6(a) but with one important and unintended difference, which meant that the nuclear-spin transitions could not be manipulated using on-chip NMR signals but instead were manipulated using the much less reported technique of nuclear electric resonance

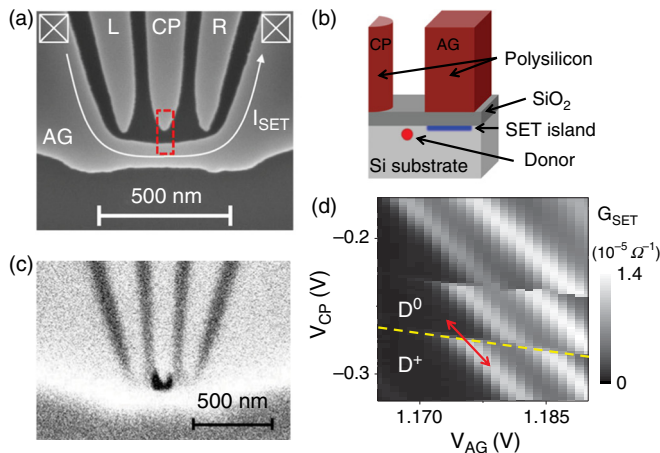


FIG. 10. Antimony spin qubit device structure and associated charge transitions. (a) Scanning electron micrograph of a typical device structure showing the polysilicon gates on SiO₂ used to form a Si SET. (b) Schematic cross-section of the device. (c) SEM image showing alignment of the window in the PMMA mask for Sb implantation with respect to the polysilicon gates. (d) Conductance of the SET, G_{SET} , vs voltages on gates AG and CP, V_{AG} and V_{CP} . The yellow dashed line indicates a donor charge transition from ionized (D^+) to neutral (D^0). The red arrow shows the direction of gate voltage pulsing used to load or ionize the donor for spin readout. Reproduced with permission from Tracy *et al.*, Appl. Phys. Lett. **103**, 114115 (2013). Copyright 2013 AIP Publishing LLC.

(NER).⁷⁷ In the micrograph, the SET and donor gates can be seen in the top right while the microwave antenna is in the bottom left of the figure. At some stage early in the operational life of the device, an electrostatic discharge damaged the antenna, creating the gap that can be seen in the structure and allowing only a time varying electric field to be applied to manipulate the spin-state of the donor.

In the presence of the externally applied magnetic field, B_0 , the nuclear spin states are Zeeman split as indicated by the green lines in Fig. 11(b). There is an additional energy shift (blue lines) due to a static electric quadrupole interaction, Q_{∞} which arises from an induced electric field gradient in the device due to lattice strain. This results in a quadrupole splitting of the nuclear resonance frequencies, f_Q [Fig. 11(c)], which makes the transitions individually addressable. Based on detailed analysis of the device characteristics and microscopic modeling of the relationship between strain and quadrupole splitting for the Sb-donor, the strain profile in Fig. 11(d) was determined.

Application of an RF electric field modulates the nuclear quadrupole energies and induces transitions between the nuclear spin states. As a consequence of the selection rules for electric quadrupole transitions (see the paper for details), the $m_I = -1/2 \leftrightarrow +1/2$ transition is forbidden in NER, and its transition rate is expected to be zero. This is verified in the experimental NER spectrum of $\Delta m_I = \pm 1$ transitions in Fig. 12(a), which shows six sharp resonances separated by $f_Q = 66$ kHz with the $m_I = -1/2 \leftrightarrow +1/2$ transition being absent. The Rabi frequencies of the $\Delta m_I = \pm 1$ transitions are shown in Fig. 12(b) with the measured values indicated by open circles that are color-coded to match the transitions in part (a). The theoretical predictions for NER transitions and for NMR transitions are indicated by stars and triangles, respectively, providing confirmation that the transitions are indeed electric-field driven. Part (c) of the figure shows nuclear Rabi oscillations for the $m_I = +5/2 \leftrightarrow +7/2$ transition. The pure dephasing time for this transition for the ionized donor was found to be $T_{2q}^* = (92 \pm 8)$ ms, which is somewhat shorter than that measured for ³¹P in a similar device, and the authors postulated that this could be due to the fact that the ³¹P has zero quadrupole moment; therefore, the shorter ¹²³Sb-coherence time may indicate that it is more susceptible to electrical noise. Nevertheless, this is still a thoroughly favorable T_2^* for quantum computing applications, and the NER control of an ¹²³Sb-qubit, $I = 7/2$, in Si opens up new possibilities for quantum computer development, including local control of individual donors using electric fields, and it also provides access to an expanded Hilbert space that offers new degrees of freedom. There is also interest in Sb:Si qubits for the possibility of exploring the quantum-classical boundary and quantum-chaotic dynamics at the level of a single nuclear spin.⁷⁸

In earlier work on As donors in bulk-Si, Franke *et al.*⁷⁹ also reported observation of quadrupole effects on the nuclear spins of neutral As-donors and noted the role of electric field gradients created due to changes in the electron wave-function under strain. As-donors in Si are well-behaved and most likely perfectly suitable for formation of donor qubits but while there have been a number of other bulk studies of As:Si for quantum computing,^{80–83} there have been no reports of isolated As-donor qubit devices.

In the literature, there has also been considerable discussion of the possibilities Bi-donors would offer as qubits.^{84–87} ²⁰⁹Bi with a nuclear-spin, $I = 9/2$, also offers the potential to access a relatively large Hilbert space. Bi also has the advantage that for relatively small applied magnetic fields, it is possible to find field values for which the

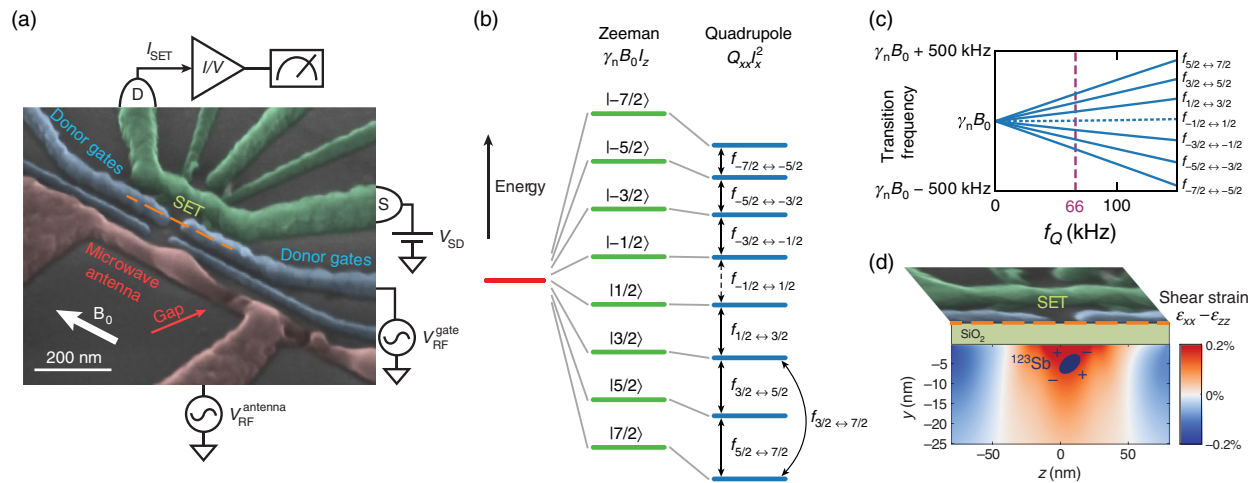


FIG. 11. An ^{123}Sb -donor- ^{28}Si matrix qubit device. (a) SEM micrograph of the device showing the SET and donor gates (upper right) and the damaged microwave antenna (lower left). (b) Energy-level diagram of the spin-7/2 nucleus of an ionized ^{123}Sb -donor. The magnetic field, B_0 , introduces a Zeeman splitting (green dashes), and the electric quadrupole interaction, Q_{xx} , produces a further energy shift (blue dashes). (c) Nuclear spin transition frequencies as a function of Q_{xx} . A non-zero Q_{xx} results in seven individually addressable nuclear resonances since the $m_I = -1/2 \leftrightarrow +1/2$ transition [blue dashed line in (c) is forbidden in NER]. The measured quadrupole splitting $f_Q = 66$ kHz is indicated by a purple dashed line. (d) Shear strain in the silicon substrate, calculated for a vertical cross-section through the device under the orange dashed line in (a). Reproduced with permission from Asaad *et al.* Nature **579**, 205 (2020). Copyright 2020 Springer.

transition frequencies are relatively insensitive to changes in the magnetic field, i.e., where $df/dB \rightarrow 0$.^{84,85} These transitions are referred to as clock transitions. They are accessible in the low-field region for both ESR (~ 10 – 200 mT) and NMR (>300 mT) transitions.⁸⁵ Again, isolated Bi-donor qubit devices have not yet been realized and Bi as an implant species is not as well-behaved as the above-mentioned donors, so there is still developmental work to be done.⁸⁷

1. Summary

Donor-based qubits in ^{28}Si lattices offer attributes that are very desirable for quantum computing applications including very long coherence times and high fidelities for gate operations. P- ^{28}Si qubit devices fabricated by the ion implantation pathway clearly satisfy the DiVincenzo criteria for individual qubits and qubit control using a number of different protocols have been demonstrated. Conditional control and quantum operation of a pair of ion implanted exchange coupled P-donor spins in a ^{28}Si epi-layer device have also been demonstrated. While donor-based qubits other than P:Si have not been as heavily explored yet, species such as Sb offer new possibilities for qubit control such as via application of electric fields, and they also offer more degrees of freedom through access to a larger Hilbert space, while P:Si has been the proving ground for donor-based qubit development in Si and is likely to continue to be the dominate player in the field for the foreseeable future dopants such as Sb and Bi and the possibilities they represent are being actively researched.

III. DONOR QUBIT FABRICATION BY ION IMPLANTATION

Ion implantation is a central tool in semiconductor device fabrication. It is used to controllably introduce dopants into semiconductor materials, providing excellent control over the spatial distributions and concentrations of implanted dopants. Being able to leverage the enormous

device processing know-how and infrastructure that has been built up in the semiconductor industry over many years is of distinct advantage for development of donor-base spin qubits in Si. Supporting electronics can also be integrated into the chip alongside the qubit devices. As conventional MOSFET device dimensions continue to shrink, greater demands are placed on implanted donor placement and number and some common challenges arise in the fabrication of ever-shrinking conventional devices and the fabrication and scale-up of donor-based qubit devices.

In this section, we introduce the main concepts of implantation and how it has been used for qubit formation in silicon. Implantation-related processes such as donor activation and diffusion are discussed in the context of donor placement precision. Promising strategies for donor qubit scale-up using single ion implantation technology are also discussed. These deterministic doping strategies aim to provide precise control over the number and position of individual implanted ions, offering the highest fidelity in spin-qubit formation and offering a promising route to scale-up of qubit architectures.

A. Ion implantation

Ion implantation involves the acceleration of charged particles, which are then directed at the target substrate that is to be implanted. The passage of the ion into the target is a stochastic process involving energy loss through both electronic and nuclear interactions and resulting in the ion deviating from its initial trajectory as it slows down and comes to rest. The final resting place of the ion within the substrate can be represented by a probability distribution like those shown in Fig. 13 for ions implanted into a Si target. These particular profiles were generated using the Monte Carlo simulation codes SRIM⁸⁸ or Crystal-TRIM⁸⁹ that have been developed over many years to accurately simulate the trajectories of ions in matter. SRIM assumes an amorphous target, while Crystal-TRIM takes into account the crystal structure of the target. More sophisticated molecular dynamics

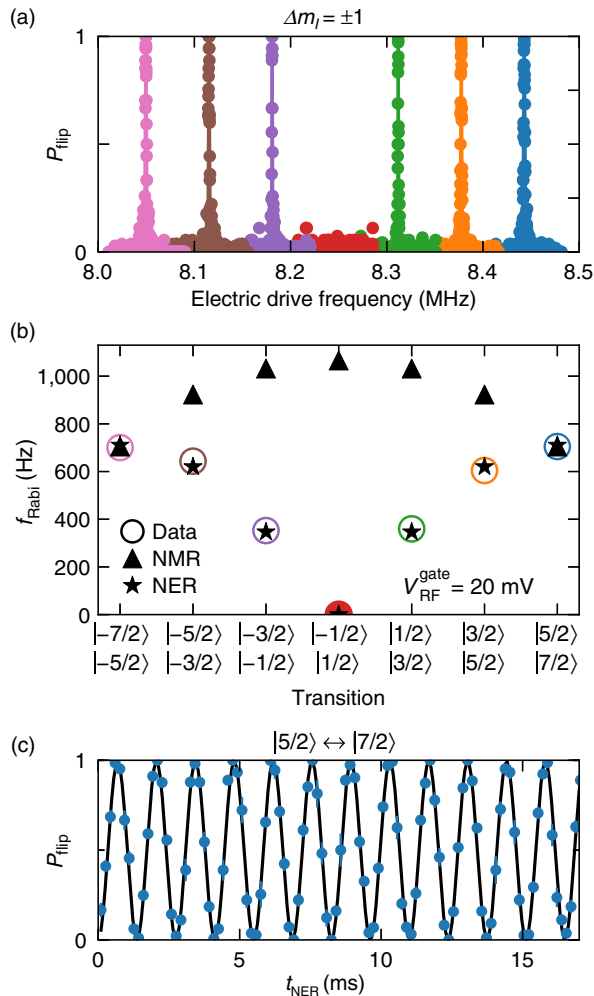


FIG. 12. (a) NER spectrum of $\Delta m_l = \pm 1$ transitions for the ^{123}Sb -donor qubit. (b) Rabi frequencies of the $\Delta m_l = \pm 1$ transitions, each measured at a constant NER drive amplitude. Measured values [open circles color-coded to match the transitions in (a)] are compared to the theoretical predictions for NER (stars) and NMR (triangles). (c) Nuclear Rabi oscillations on the $m_l = +5/2 \leftrightarrow +7/2$ transition. Adapted with permission from Asaad *et al.*, *Nature* **579**, 205 (2020). Copyright 2020 Springer.

simulations have also been employed to explore and optimize the parameter space for implantation.^{90,91}

Ion channeling occurs when the implanted ion is guided along a major crystallographic direction or channel in the Si substrate. The effects of channeling can most clearly be seen in the 2D Crystal-TRIM simulations in Fig. 13(c), where, in particular, the P implant distribution shows clear evidence of branches that extend along major crystallographic directions in the substrate. These can also be seen to a smaller extent in the As distribution. The impact of ion channeling on the ion distribution is also dramatically evident in Fig. 13(a) where the implantation profile represented by the solid line labeled C-TRIM (chan, no oxide) shows how ion channeling produces an implant distribution that extends over a much greater distance into the substrate than the corresponding implant into an amorphous structure as depicted by the SRIM or the C-TRIM (ran) profiles (“ran” here refers

to implantation along a non-crystallographic or random direction in the lattice, which produces a similar implant profile to that achieved by implantation into an amorphous target). The projected range (depth at maximum concentration) for 14 keV P implanted into amorphous Si, or equivalently along a random direction into crystalline Si, is in the range $R_p = 17.8\text{--}22.8$ nm depending on the model used. The straggle, ΔR_p , the variance in ion depth, is around 10 nm for this particular implant. Figure 13(a) also shows how an oxide layer on the surface of the Si crystal greatly reduces the probability of channeling implantation, as evident from the profile labeled C-TRIM (chan).

Figure 13(b) shows the variation in ion range straggling for a number of common implant species in Si. Here, the ion energy has been selected to achieve a similar projected range. The ion range straggle can be an important consideration when wanting to place implanted donors within proximity to surface gates and SET islands, for example, and this is an area where the heavier implant species have a clear advantage. While neither of these Monte Carlo codes consider dynamic effects such as the accumulation of damage or thermodynamic processes taking place within the target those are secondary considerations and the codes do capture the stochastic nature of the ion implantation process extremely well and have been extensively used in modeling implant distributions for device design in the semiconductor industry over many years. For qubit device applications, the need for accurate models of the implantation process is often even greater since the concentrations of donors are often well below the detection limits of standard characterization techniques and hence there is a strong reliance on the models accurately predicting the final implant profile.

B. Post-implant processing

During device fabrication, the Si will undergo various high temperature processes. This is mentioned here since it will further impact the placement accuracy of the implanted dopant. The two main processes are thermal oxidation to form a high-quality surface oxide to isolate the donor from top electrical gates and donor activation to electrical activate the donor spin qubit. Both vacancies and interstitials will mediate dopant diffusion, giving rise to complex dopant redistribution. Theories on dopant-defect interactions are then central to modeling efforts. This is especially important when describing the evolution of ion implanted profiles where a non-equilibrium concentration of defects are introduced.

Si-interstitials injected from the Si/SiO₂ interface into the substrate during oxidation can interact with implanted donors such as P, which predominantly diffuses via an interstitial based mechanism and may result in oxidation enhanced diffusion (OED). To avoid donor diffusion during gate oxide growth and also to decrease the probability of ion channeling during implantation, it is often preferable to grow the gate oxide prior to implantation. This is particularly true for P-donor qubits, for example.^{92,93} When the SiO₂ interface trap density is initially high, these implants can in fact be beneficial. These interfacial defects consist of Si dangling bonds (paramagnetic Pb centers). It is important to keep these at a minimum so that device function is not compromised. Heavier ions will have a greater impact on the trap density. However, several of the heavier implant species of interest for qubit formation tend to have lower diffusion coefficients than P and hence oxidation after implantation may be considered.^{40,94–96} The larger ions also tend to be vacancy-based diffusers with Bi even displaying oxidation-retarded diffusion.⁹⁷

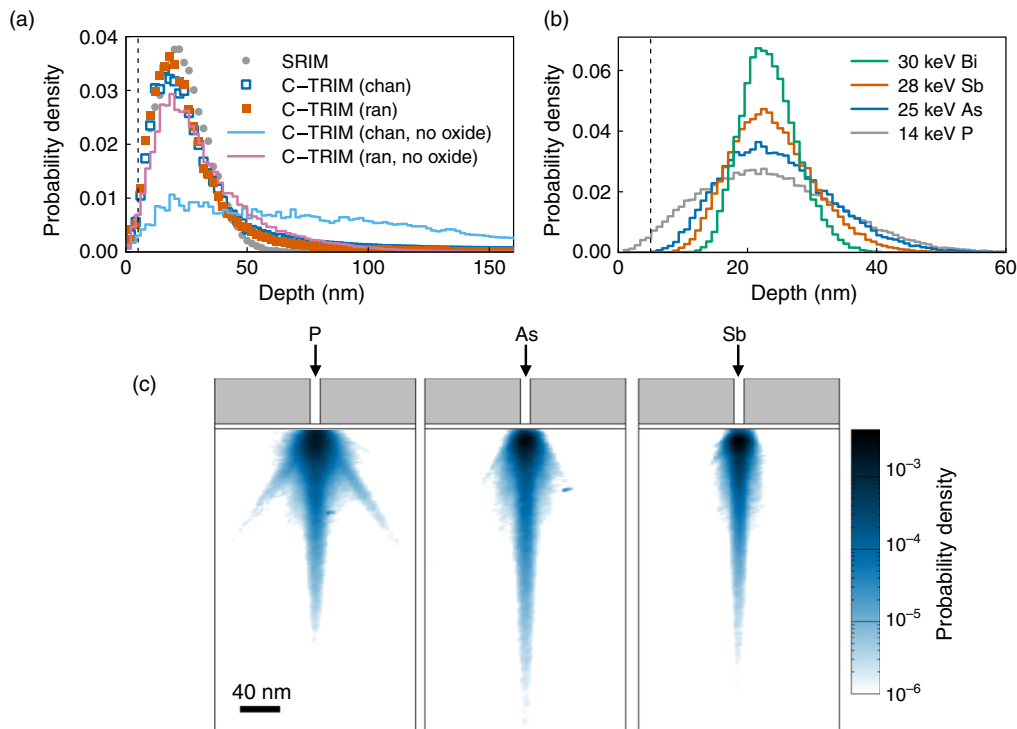


FIG. 13. (a) Monte Carlo simulations of 14 keV P implanted into Si in both random and channeled directions showing implantation through an oxide (data points) and without a surface oxide (solid lines). The sample rotation and tilt for the random and channeled orientations are $(\theta, \phi) = (10^\circ, 7^\circ)$ and $(0^\circ, 0^\circ)$, respectively. SRIM simulations are shown for comparison. (b) Comparison of the ion range straggling for P, As, Sb, and Bi simulated with SRIM. (c) 2D Crystal-TRIM simulations of P, As and Sb through a 5 nm surface oxide. A implant mask containing a 10 nm window is used. The color scale has been plotted on a log scale to exaggerate the channeled component of the implants.

After implantation, thermal processing is used to both electrically activate the implanted donors and repair any damage from collision cascades generated during donor passage into the Si lattice. The fluences employed for qubit formation are generally well below the amorphization threshold of silicon. This is in contrast to front-end CMOS processing where donor concentrations for shallow junction formation regularly exceed the amorphization threshold.

For low fluence P implantation, the electrical activation is expected to be close to 100%. However, dopants such as Sb and Bi with their lower solid solubility have a lower activation yield.⁹⁸ Low concentrations of near-surface Bi donors have been found to have an electrical activation yield of around 30%.⁸⁷ Higher yields have been observed with Bi donors implanted deeper into the Si or higher Bi concentrations.^{87,99} This may suggest that interactions between the implanted donors with the surface or with the annealing ambient may inhibit complete donor activation. Stress due to over-layers may also modify the diffusion kinetics. These questions are ongoing areas of basic research that support the further development of both classical and quantum CMOS processing.

C. Deterministic ion implantation

For all of the donor-qubit devices presented in Sec. II, an ensemble of donors were implanted through an implantation mask. For the P-donor devices, the ion implantation step was performed after gate oxide growth but prior to deposition of the gate electrodes. Typically

an implant window of $\sim 90 \times 90 \text{ nm}^2$ was used, and the fluence was chosen so that $\sim 20 - 30$ donors would be implanted within the implant window and at sufficient depth below the oxide-Si interface that a number of them would be addressable by the gate electrodes and within favorable tunneling distance to the SET island. The implant configuration is shown schematically in Fig. 14.

To develop a scalable donor qubit fabrication strategy with controllable coupling between adjacent donors ideally, one would like to be able to deterministically implant individual donors in a series of adjacent implant windows at favorable separations with each implant window being sequentially exposed to the beam. However, for a fixed beam current, the number of ions implanted through an implant window within a given time interval is determined by Poissonian statistics. Therefore, if the beam current is tuned to give one ion per time interval on average into the implant window, then there will be a 36.8% probability that one ion will be implanted through each implant window. The probability of implanting two ions in adjacent devices then becomes 13.5%, with more complex devices giving diminishing yields. Although a higher average number of donors can be implanted in each window to minimize the chance of not implanting a donor at all, this gives rise to the possibility that more than one donor will be implanted in each window, adding to device variability, and although the device gate voltages can often be tuned to ensure a single P atom is addressed,^{16,39,48,70,71} this is not a sustainable pathway for large-scale device fabrication.

To scale-up qubit devices, minimize variability/complexity, and increase device yield, deterministic implantation has been developed.

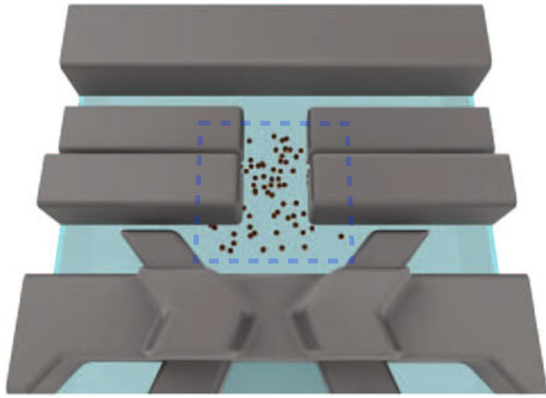


FIG. 14. Schematic of an ion implanted P-donor qubit device similar to those presented in Sec. II. The boundary of the $\sim 90 \times 90 \text{ nm}^2$ implant window formed using a lithographic masking process is illustrated by the dashed line. The implantation step occurs after gate oxide growth but prior to gate electrode deposition. Typical P-implant fluences of $\sim 1 \times 10^{11} \text{ cm}^{-2}$ are used in these device structures to achieve isolated P-donors, and for the exchange coupled P-donor device, a higher fluence of $\sim 1.25 \times 10^{12} \text{ cm}^{-2}$ was used to ensure a reasonable statistical probability that two donors would be fortuitously located in a favorable exchange coupled configuration. Adapted with permission from Mądzik *et al.*, Nat. Commun. 12, 181 (2021). Copyright 2017 Author(s), licensed under a Creative Commons Attribution (CC BY) license.

Even in conventional transistors, variations in donor number can result in threshold voltage shift deviations.¹⁰⁰ This can be mitigated by counted implants in ordered donor arrays.¹⁰¹ Deterministic ion implantation is extremely important for scale-up to multiple donor qubit architectures by allowing controllable counting of individual ions or groups of ions into precisely controlled locations within the substrate to form individual qubits and qubit arrays. Various routes have been identified to achieve this, which are summarized below.

1. Atom counting

Various techniques have been developed to allow the number of implanted ions to be counted. On entering the Si, the energy of the implanted ion is lost to the target via both electron and nuclear stopping processes. The electronic stopping process imparts kinetic energy to electrons in the target, which form electron-hole pairs. In addition, a small fraction of electrons created during impact are emitted from the surface producing secondary electrons that can be detected.^{102–104} For single ion impacts, the secondary electron yield can be quite low, but it can be enhanced by employing highly charged ions.¹⁰⁵ However, any existing resist on the Si surface or apertures placed close to the Si target can certainly attenuate the signal, and if a gate oxide is present, this detection method will not allow ions that stop in the oxide, and therefore cannot be electrically activated, to be differentiated from those that stop in the substrate and can form qubits.

The electron-hole pairs created as the ion loses energy and comes to rest in the substrate can also be separated and collected to form a measurable electrical signal when an electric field is applied within the target. In this instance, the target must have appropriate detector electrodes incorporated. A major advantage of this technique is that only ions that enter the active volume of the device produce a signal. Ions that interact only with the surface oxide or resist layer, for example, will not register on the detection electronics. Various detector designs

have been implemented such as PiN junctions¹⁹ and Geiger mode avalanche diode detectors.^{106–109}

These demonstrations of single qubit devices using the electron-hole pair detection strategy have shown that detector electrode geometries can be incorporated that can still accommodate the subsequent formation of qubit control gates despite the more complex fabrication process. After implantation, the implanted donor qubits must be electrically activated with thermal processing as described above. If the detector electrodes cannot withstand the donor activation anneal, they must be removed before further processing and patterning of qubit control gates. Devices consisting of poly silicon gates have a higher thermal stability and may greatly simplify processing as demonstrated with Er implanted into full fabricated finFET devices^{110,111} or the Sb implanted devices of Tracy *et al.*⁴⁰

The detection of single ions can also be achieved with sub-micrometer-scale transistors.^{100,112–114} In devices such as finFETs, the source-drain current flow is confined to a small volume and is therefore very sensitive to charge generated in the device. Instead of a transient signal arising from the generation of electron-hole pairs, steps in the source-drain current are observed. This is possibly due to the formation of defects in the transistor channel and Si/SiO₂ interface defects, which increases the channel resistance and the threshold voltage swing. Multiple low energy single ion implants cause further degradation of the device and decrease the step height contrast, which may limit the utility of this pathway for formation of qubit arrays. Nevertheless, the robustness of finFET devices under implantation and the ability to post-process then to activate implanted species has been demonstrated even for such heavy ions as Er.^{110,111}

Creating a non-Poissonian ion beam can also be realized with a Paul trap type implanter.^{115–117} The atom trap consists of a linear array of electrodes between which Ca ions are carefully loaded via photo-ionization and laser cooling. The ions can be individually counted via monitoring their fluorescence and extracted from the trap with a specific accelerating voltage individually. The fidelity of this process has been reported to be about of 96%.¹¹⁷ Non-fluorescing ions can also be identified when placed between two Ca ions due to their absence of fluorescence.¹¹⁵

2. Spatial control

Both detector types mentioned above allow for ions to come to rest within a construction zone defined lithographically with patterned resist on the Si surface. For unmasked implantation, the ion beam spot size itself must be sufficiently small to direct the ions just to the active device. To achieve this, the ion beam can be constrained with ion optics,¹⁰⁹ or a broader beam can be directed onto a nano-aperture, which can be scanned across the substrate by mounting it on a piezo-electric stack or incorporating it into an atomic force microscope (AFM) cantilever, as illustrated in Fig. 15.^{118,119} The AFM approach allows registration of the implant area to markers outside of the construction zone. Implanted regions can also be imaged with an AFM after implantation if an appropriate surface resist is used such as CR-39, a plastic nuclear track detector,¹²⁰ or even PMMA.¹²¹

D. Summary

A combination of both atom counting and spatial control techniques offers the highest fidelity for deterministic ion implantation.

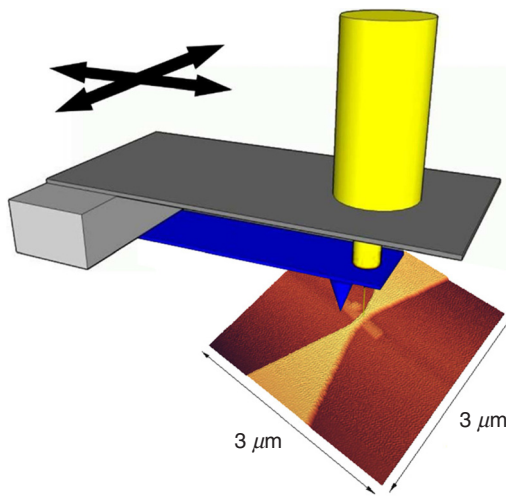


FIG. 15. Schematic of the setup for ion implantation through a scanning nano-aperture with *in situ* non-contact scanning atomic force microscope imaging of structures on the substrate for alignment purposes. The ion beam is represented in yellow, while the AFM cantilever with the nano-aperture incorporated in it is shown in dark blue. Above the cantilever, a further collimating aperture is illustrated in dark gray. Reproduced with permission from Ilg *et al.*, J. Vac. Sci. Technol. B **30**, 06FD04 (2012). Copyright 2012 American Vacuum Society.

This technology is still being developed but certainly moving toward the fidelities required for large scale donor spin qubit arrays.

IV. IMPLANTATION SCALE-UP PATHWAYS

In Secs. II and III, we reviewed the attractive attributes of implanted single donor spin qubits in silicon and how ion implantation can be used in the fabrication of donor qubit devices in Si, but it remains an outstanding challenge to identify a suitable process flow for scale-up to build a multi-qubit processor, let alone couple two donor spins with high-fidelity to perform quantum operations in a controllable and reproducible manner.

Naturally, donor bound electron spins can interact via their magnetic dipole or via the exchange interaction between neighboring spins. The small magnetic dipole of the electron spin results in slow two qubit gates^{24,122} and is therefore less attractive for a competitive scale-up pathway. Depending on the wave-function overlap, the exchange interaction can admittedly be several gigahertz, resulting in sub-nanosecond two qubit gate operation times, but it is accompanied by tight fabrication requirements due to the small Bohr radius of the donor. This short range interaction can be harnessed to prototypically demonstrate two qubit logic gates,¹⁷ but it is generally recognized that those tight requirements have to be relaxed to realistically scale-up donor qubit devices by either finding strategies that are less sensitive to precise donor placements or architectures that allow for mid-to-long range couplings. In recent years, there has been a variety of proposals to advance on the original Kane architecture³⁷ and address the challenge of scale-up by either using a new qubit encoding, different coupling strategies, or different architectures.

In Subsections IV A–IV D, we will review and discuss those pathways for scaling up implanted donor devices to experimentally achieve high fidelity two qubit operations. We first focus on strategies uniquely

developed for donor spins and will then discuss more general proposals for scale-up that can be applied to this type of qubit system as well.

A. J -coupled qubits

Two qubit logic gates for implanted donor electron spins in silicon can be performed using the exchange interaction, J , between two qubits, given by the wavefunction overlap and the Heisenberg exchange interaction. Depending on the ratio of J to the energy splitting of the qubits, a two qubit gate can be implemented in three different ways. Two of these strategies, the SWAP and Controlled-Z, where J exceeds the energy detuning, require dynamical control of the exchange, i.e., a way to switch on the interaction for a certain amount of time, and are hence difficult to realize for the electron spins, tightly bound to the donor nucleus. The third method,¹²³ applicable when J is smaller than the qubits' detuning, constitutes a controlled rotation (CROT) employing a single qubit ESR π -pulse on the target qubit whose resonance frequency is conditional upon the state of the control qubit. This was initially discussed in Sec. II for the exchange coupled qubit work of Mądzik *et al.*¹⁷ The CROT gate neither requires control nor an exact value of the spin exchange and can be implemented in a broad range of J values, ranging from the resonance linewidth of a few kilohertz to the hyperfine coupling $A \approx 117$ MHz, when the energy splitting is given by the anti-parallel nuclear spin states.

Given the small in Bohr radius of approximately 2 nm for donor electron spins, the fact that the exchange interaction decreases exponentially with distance and the inherent uncertainty in the position of the implanted donors of about a few nanometers for typical donor qubit device implants, experimentally realizing reliable two-qubit gates based on the exchange interaction is challenging. Furthermore, the strength of the exchange interaction oscillates on the scale of the lattice constant due to valley interference of the silicon host material. Nevertheless, using the right ion implantation strategy¹⁷ allows a conditional two qubit quantum operation to be demonstrated in the regime where the exchange $J = 32$ MHz is smaller than the hyperfine interaction $A = 90$ MHz. As discussed above, in this case, a two qubit CROT gate can be performed by a single qubit ESR π -pulse on the target qubit and is insensitive to the precise value of J .

Figure 16(a) shows the simulated spectrum of a J -coupled donor pair as a function of frequency and strength of the exchange. It shows six main ESR resonances and several faint “sister”-transitions. Here, we focus on two of the four ESR peaks that are shown in the measured ESR spectrum for the target qubit in Fig. 16(b), namely, the ones whose Rabi oscillations are shown in Figs. 16(c) and 16(e). Those resonances occur for the target qubit if the nuclear states are aligned anti-parallel and the control qubit is in the $|\downarrow\rangle$ state. The two qubit CROT gate can be realized by a π -pulse on these transitions, e.g., at approximately 5 μ s in Fig. 16(c). The reason for the limited visibility for conditional Rabi oscillations compared to the trivial case is currently unknown.

Nevertheless, a scale-up pathway solely based on the exchange interaction has little realistic prospect of success, especially given the tight confinement of donor bound electron spins and the exponentially decaying interaction strength.

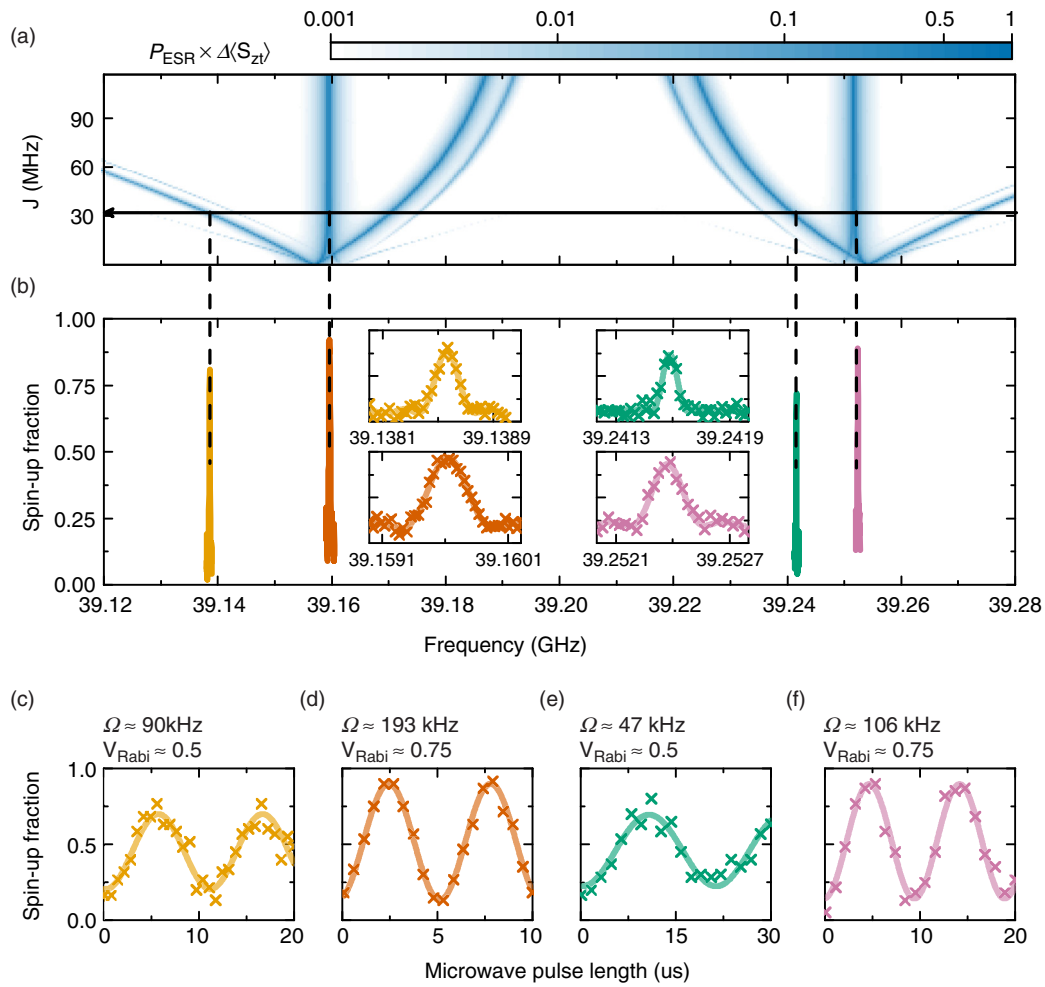


FIG. 16. Two qubit CROT gates: (a) The simulated ESR spectrum of two J -coupled donor pairs as a function of the exchange interaction strength shows six main resonances and several “sister” transitions. (b) The measured ESR spectrum for the target qubit shows four distinct ESR peaks. The control electron is kept in the ground state and the nuclear configuration is initialized using NMR pulses. (c)–(f) Rabi oscillations for the target electron for all four resonances show varying Rabi frequencies and visibility. The oscillations in (c) and (e) are conditional on the state of the control electron and a π -pulse constitutes a two qubit CROT gate. Adapted with permission from Mądzik *et al.*, Nat. Commun. **12**, 181 (2021). Copyright 2017 Author(s), licensed under a Creative Commons Attribution (CC BY) License.

B. Flip flop qubit

To mitigate the challenging fabrication requirements for J -coupled qubits, Tosi *et al.*¹²⁴ proposed a novel kind of logical qubit encoding for implanted donor-based quantum devices. The key idea here is to employ the so-called flip-flop states, the anti-parallel $|\downarrow\uparrow\rangle$ and $|\uparrow\downarrow\rangle$ spin configuration of the electron–nuclear pair, as the qubit’s basis states. Here, \downarrow, \uparrow (\downarrow, \uparrow) represent the electron (nuclear) spin orientation. Additionally, the donor electron is tunnel-coupled to an interface quantum dot, formed beneath the donor top gate as depicted in Fig. 17(a). Modulating the hyperfine interaction, A , that couples the electron and nuclear states using an electric drive tone that periodically moves the electron relative to the donor, induces an electric dipole spin resonance (EDSR) transition between the basis states $|\downarrow\uparrow\rangle$ and $|\uparrow\downarrow\rangle$, see Fig. 17(c). The EDSR drive strength is given by the electric field dependence of the hyperfine interaction and can be increased by statically displacing the

electron away from the donor using a DC voltage on a gate electrode on top of the donor [Fig. 17(a)]. The highest drive strength can be achieved if the electron is moved halfway to the ionization point, i.e., the point in voltage space where the donor is ionized [(Fig. 17(b)). Although it appears that the qubit is most sensitive to charge noise here, it turns out that for the right tunnel coupling to the interface quantum dot, a second order clock transition (first two derivatives of the energy splitting with regard to the electric field are zero) emerges. Leveraging this charge noise insensitivity and the strong electric drive at this point, single qubit gates with an average gate error below 10^{-3} including state-of-the-art charge noise levels for silicon quantum devices can be achieved.

The heart of the flip flop proposal lies with two qubit gates. Displacing the negatively charged electron away from the positively charged nucleus creates an electric dipole of order 100 D whose

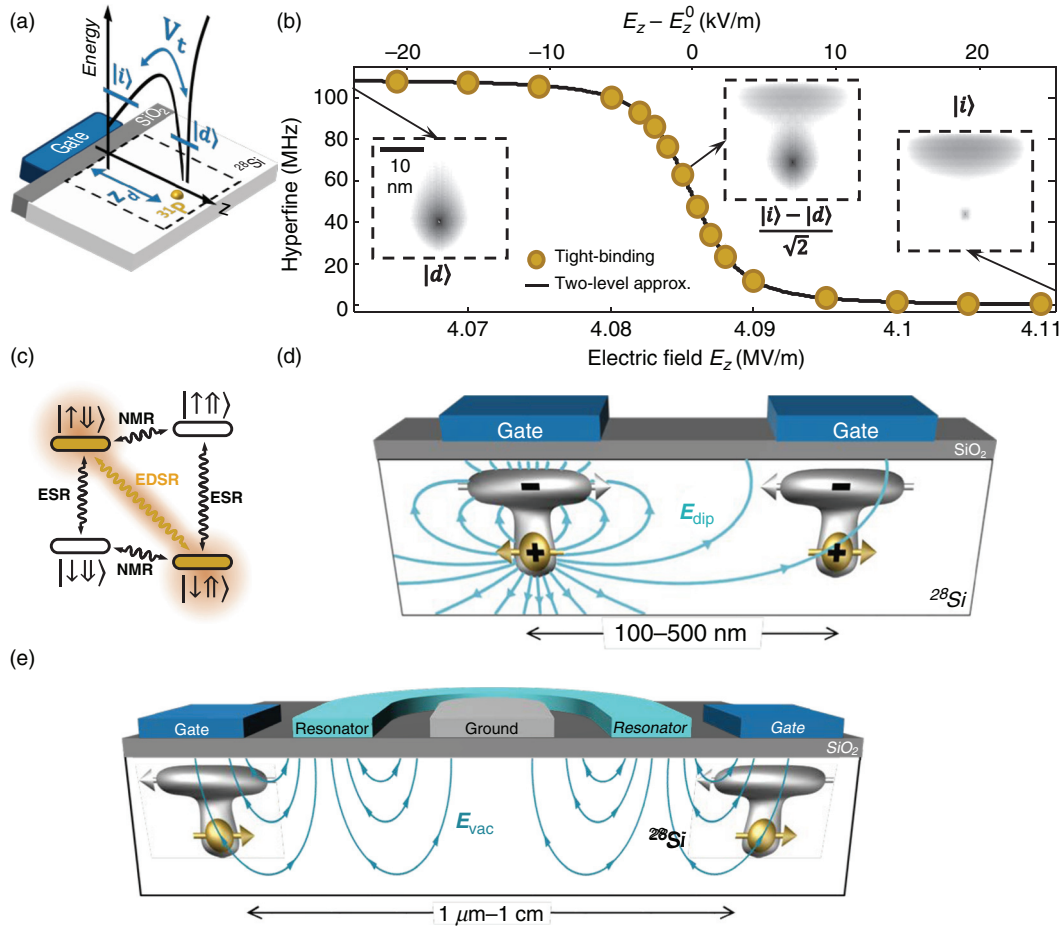


FIG. 17. Flip flop qubit: (a) The flip-flop qubit is a spin-charge hybrid qubit formed by the anti-parallel nuclear and electric spin states while the electron is shared between the donor $|d\rangle$ and an interface quantum dot $|i\rangle$. (b) The hyperfine interaction A becomes susceptible to electric fields when the electron is detuned from the donor. (c) Transitions between the basis states, $|\uparrow\uparrow\rangle$ and $|\downarrow\downarrow\rangle$, can be driven via hyperfine mediated EDSR. (d) Displacing the electron away from the nucleus creates an electric dipole that couples qubits up to 500 nm apart. (e) The flip flop states can be coupled to microwave photons residing in a superconducting resonator, which increases the coupling distance to the centimeter range. Adapted with permission from Tosi *et al.*, Nat. Commun. 8, 450 (2017). Copyright 2017 Author(s), licensed under a Creative Commons Attribution (CC BY) License.

interaction range only decreases with $1/r^3$, where r is the distance between two dipoles. As the dipole is furthermore aligned vertically and hence not screened by the gate electrode, flip flop qubits can be coupled over hundreds of nanometers via the dipole interaction. Figure 17(d) depicts a schematic of this interaction. Tosi *et al.*¹²⁴ predicted two qubit \sqrt{i} SWAP gates with average gate errors below 1% within 50 ns for a coupling distance of 200 nm.

1. Coupling to microwave photons

In general, the weak magnetic dipole coupling of the donor spins [of order 3 kHz (Ref. 125)] renders a direct magnetic coupling to microwave photons inside a superconducting resonator difficult to achieve experimentally. However, the flip flop qubit encoding takes advantage of the large electric dipole to electrically couple the spin states to microwave photons confined in a superconducting resonator,

as schematically shown in Fig. 17(e). This way, even longer interaction distances of order centimeters can be achieved. Two qubit gates can be performed between flip flop qubits positioned at half the photon wavelength along the resonator by switching on their respective dipole, i.e., by displacing the electron from the nucleus. A theoretical coupling strength of $g \approx 3$ MHz between the flip flop state and the photon¹²⁴ allows for a realistic prospect to achieve the strong coupling regime using high quality, high kinetic inductance resonators.

Note that exploiting the artificially created electric dipole interaction in the flip flop qubit encoding additionally allows for a strong coupling (of order 1 MHz) between the nuclear spin and cavity photons. This is achieved by driving the nuclear transition with a combined magnetic and electric drive in a Raman-like process.¹²⁶ Slightly detuned from resonance, the magnetic tone drives the pure electron transition, whereas the electric tone drives the flip flop transition resulting in a second order drive of the nuclear transition. This way,

the electric dipole opens up cavity quantum electrodynamics control techniques and scale-up pathways to the nuclear spins of implanted phosphorous donors, in analogy to the flip flop qubit.

C. Additional couplings strategies

In the following, we discuss alternative coupling strategies and architectures for scaling up implanted donor spin qubits. Not all of them are uniquely designed for this qubit system but can be applied nonetheless.

To space out spin carrying electrons and create room for interconnects or cryogenic control hardware, the electrons can either be physically moved, i.e., shuttling the confinement or via coherent transport by adiabatic passage (CTAP), or the spin can be coupled via mediators, such as spin chains, intermediate quantum dots, ferromagnets, or photons.

1. Donor spin qubit architectures

As one of the first extensions of the Kane architecture, Hollenberg *et al.*¹²⁷ proposed to overcome the short range coupling issues associated with the exchange interaction by using electron shuttling via CTAP to relax the tolerances required for device fabrication. The qubit architecture is divided into interaction regions carrying out logic gate operations via the canonical *A* and *J* gates, storage zones where quantum information is transferred to long-lived ionized donors and shuttling zones.

O’Gorman *et al.*¹²⁸ proposed a surface code quantum computer for donor spins in silicon that abandons direct inter-qubit gates and is less demanding on donor placement precision but instead requires parity readout of four neighboring spins. The proposed architecture consists of two qubit planes separated by 40 nm, one containing a two dimensional grid of data qubits and the other a two dimensional grid of donor spin qubits used as magnetic probes, both with a 400 nm qubit pitch. The two planes are continually shifted relative to each other in a cyclic motion such that a parity measurement of a set of four data qubits can be achieved by a state dependent phase shift that occurs due to the dipole interaction between the data qubit and the probe.

A donor-quantum dot hybrid architecture that combines donor nuclear spins as quantum memories and donor electron spins and electron spins confined in interface quantum dots coupled to each other via exchange interaction has been proposed by Schenkel *et al.*¹²⁹ Quantum information is transferred between the donor nuclear and donor electron spin via the hyperfine interaction and between the donor electron spin and the spin of an electron in the quantum dot by the exchange interaction. Electrostatic gating is used to select between these interaction pathways. First experimental steps toward donor-quantum dot hybrids have recently been demonstrated. Urdampilleta *et al.*¹³⁰ demonstrated charge dynamics and Pauli blockade in a silicon nanowire corner quantum dot coupled to a single P atom. First coherent operations of a P donor coupled to a gate defined interface quantum dot operated as a singlet-triplet qubit have been experimentally demonstrated in Ref. 131.

Another alternative route to building a scalable donor spin qubit architecture is to leverage the optical properties of deep chalcogen donors in silicon. Unlike shallow, hydrogenic donors such as phosphorus, chalcogen donors like sulfur, selenium, and tellurium offer large

electron binding energies of order 500 meV when singly ionized resulting in mid-infrared optical transitions. Implanted far away from the SiO₂ interface, these donors retain their bulk coherence properties, and they can be operated at low magnetic fields and high temperatures (4.2 K). Implanted at the anti-nodes of silicon photonic structures, deep chalcogen donors are suitable for cavity quantum electrodynamics-based qubit measurement and coupling schemes. First ensemble measurements of the 1s:A ground-state of singly ionized ⁷⁷Se⁺ presented in Morse *et al.*¹³² have demonstrated long relaxation and dephasing times at 4.2 K.

2. Spin chains

One dimensional spin chains have been proposed to mediate coupling between distant spin qubits in a variety of qubit systems.^{133,134} For an odd number of spin links and a strong spin-spin interaction between the links, a spin chain behaves like a spatially extended spin $\frac{1}{2}$ particle that can be used as an intermediate qubit. Using either consecutive SWAP operations between qubit and individual chain links or an adiabatic state transfer, two data qubits that are *J*-coupled to either end of the chain can interact with each other. Mohiyaddin *et al.*¹³⁵ provided a quantitative analysis for spin chains of various length (3, 5, and 7) realized by implanted donors. Given realistic uncertainties of the donor position, they found that for bulk-like donors, the inter-donor distance is only of order 5 nm as a result of the strongly confined electron wave-function. Moving the electron from the donor to a naturally occurring interface quantum dot¹³⁶ (see Sec. IV B) relaxes the donor distance to tens of nanometer and a spin chain length of 115 nm can be realized by seven donors.

3. Ferromagnets

Trifunovic *et al.*¹³⁷ have proposed a long-distance coupling scheme of order micrometers for atomistic qubits that is mediated by the magnetic dipole interaction to a gapped ferromagnet in proximity to the spin qubits. The interaction to the ferromagnetic mediator can be tuned by adjusting the qubits close to the ferromagnetic resonance and by optimizing the geometry of the coupler to a dog-bone shape. High fidelity CNOT operations for qubits that are 1 μ m apart and placed 25 nm below the ferromagnet can be realized within tens of nanoseconds.

4. Intermediate quantum dots

Elongated multi-electron quantum dots (nicknamed Jellybeans) can mediate a Ruderman–Kittel–Kasuya–Yosida-like indirect exchange coupling between spin qubits tunnel-coupled to their ends.¹³⁸ The strength of the interaction is determined by the tunnel coupling and the energy gap of the ground and excited states of the intermediate dot. The size of the mediator (>100 nm) allows for spacing out individual data qubits. Multi-electron dots have been experimentally investigated for a range of different occupancies¹³⁹ down to an empty quantum dot¹⁴⁰ in GaAs spin qubit devices.

D. Summary

The stringent requirements on donor location and inter-donor separation for exchange coupling of donor qubits are not compatible

with the tolerances available with ion implantation, and so other scale-up pathways have needed to be identified. While many alternative pathways have been proposed, the challenge now is to find which of them offer the most advantage and this is an important focus of current research.

V. CONCLUSIONS

Single donor qubits in Si possess all of the key attributes that are desirable for the fundamental building blocks of a quantum computer architecture. While much of the key research and achievement of milestones has related to P donor qubits in Si, other donor qubit systems such as Sb and Bi are also starting to be developed and have the potential to offer new degrees of freedom and new qubit control functionalities. All of the key milestones have been met through an ion implantation approach to qubit formation. While in most cases ensembles of donors have been implanted, the average inter-donor distance can be sufficiently large that isolated single donors are addressable. Increasing the implant fluence has allowed demonstration of qubit-qubit coupling and two-qubit control through measurement and manipulation of qubits that are fortuitously located at suitable sites in the lattice and in relation to each other that they are appropriately exchange coupled but can still be individually addressed using nearby gates. However, this approach to qubit coupling cannot conceivably offer a scalable pathway that is compatible with the inherent tolerances in the ion implantation process, and so alternative schemes that allow qubit coupling over distance and that are also tolerant to the degree of uncertainty in the precise location of the donor have been proposed and are now actively being developed. Deterministic doping, where individual donors are controllably implanted into the substrate at locations that are defined either through use of a highly focused beam or through use of a movable nanoaperture and where passage of the ion into the lattice is detected, is an important technology that is under development alongside the scale-up strategies. Based on the intensity of research in this field, we can reasonably expect to see key steps toward scale-up be demonstrated in the near-term starting with controlled coupling of pairs of donors over distance and then, based on the engineering knowledge obtained through this process, scale-up to larger arrays of donors can then be pursued.

Finally, returning to the DiVincenzo criteria that were introduced in Sec. II, it is clear that donor-based qubits in Si are well-characterized, can be initialized to a well-defined state, exhibit excellent coherence times that are much longer than the gate operation times, and that qubit-specific measurement capabilities are available, and, for coupled qubits, a universal gate set has been demonstrated. This satisfies DiVincenzo criteria 2–4 and most of criterion 1 with the one remaining gap being the need to demonstrate a reliable pathway for qubit scale-up, and that, as has already been noted, is where significant research effort is currently focused.

ACKNOWLEDGMENTS

B.C.J. and T.B. acknowledge funding from the Australian Research Council Centre of Excellence for Quantum Computation and Communication Technology (Project No. CE170100012) and the U.S. Army Research Office (Grant No. W911NF-17-1-0200).

DATA AVAILABILITY

Data sharing is not applicable to this article as no new data were created or analyzed in this study except for the data presented in Fig. 13, in which case the data are available from the corresponding author upon reasonable request.

REFERENCES

- ¹M. A. Nielsen and I. L. Chuang, *Quantum Computation and Quantum Information* (Cambridge University Press, 2000).
- ²D. P. DiVincenzo, "The physical implementation of quantum computation," *Fortschr. Phys.* **48**, 771 (2000).
- ³K. L. Brown, W. J. Munro, and V. M. Kendon, "Using quantum computers for quantum simulation," *Entropy* **12**, 2268 (2010).
- ⁴A. M. Childs, D. Maslov, Y. Nam, N. J. Ross, and Y. Su, "Toward the first quantum simulation with quantum speedup," *Proc. Natl. Acad. Sci. U. S. A.* **115**, 9456 (2018).
- ⁵A. J. McCaskey, Z. P. Parks, J. Jakowski, S. V. Moore, T. D. Morris, T. S. Humble, and R. C. Pooser, "Quantum chemistry as a benchmark for near-term quantum computers," *npj Quantum Inf.* **5**, 99 (2019).
- ⁶C. Monroe and J. Kim, "Scaling the ion trap quantum processor," *Science* **339**, 1164 (2013).
- ⁷M. H. Devoret and R. J. Schoelkopf, "Superconducting circuits for quantum information: An outlook," *Science* **339**, 1169 (2013).
- ⁸D. D. Awschalom, L. C. Bassett, A. S. Dzurak, E. L. Hu, and J. R. Petta, "Quantum spintronics: Engineering and manipulating atom-like spins in semiconductors," *Science* **339**, 1174 (2013).
- ⁹F. A. Zwanenburg, A. S. Dzurak, A. Morello, M. Y. Simmons, L. C. L. Hollenberg, G. Klimeck, S. Rogge, S. N. Coppersmith, and M. A. Eriksson, "Silicon quantum electronics," *Rev. Mod. Phys.* **85**, 961 (2013).
- ¹⁰R. Hanson, J. R. Petta, S. Tarucha, and L. M. K. Vandersypen, "Spins in few-electron quantum dots," *Rev. Mod. Phys.* **79**, 1217 (2007).
- ¹¹W. B. Gao, P. Fallahi, E. Togan, J. Miguel-Sanchez, and A. Imamoglu, "Observation of entanglement between a quantum dot spin and a single photon," *Nature* **491**, 426 (2013).
- ¹²T. Gaebel, M. Domhan, I. Popa, C. Wittmann, P. Neumann, F. Jelezko, J. R. Rabreau, N. Stavrias, A. D. Greentree, S. Praver, J. Meijer, J. Twamley, P. R. Hemmer, and J. Wrachtrup, "Room-temperature coherent coupling of single spins in diamond," *Nat. Phys.* **2**, 408 (2006).
- ¹³L. Robledo, L. Childress, H. Bernien, B. Hensen, P. F. A. Alkemade, and R. Hanson, "High-fidelity projective read-out of a solid-state spin quantum register," *Nature* **477**, 574 (2012).
- ¹⁴M. Steger, K. Saeeedi, M. L. W. Thewalt, J. J. L. Morton, H. Riemann, N. V. Abrosimov, P. Becker, and H.-J. Pohl, "Quantum information storage for over 180 s using donor spins in a ²⁸Si 'semiconductor vacuum,'" *Science* **336**, 1280 (2012).
- ¹⁵J. J. Pla, K. Y. Tan, J. P. Dehollain, W. H. Lim, J. J. L. Morton, D. N. Jamieson, A. S. Dzurak, and A. Morello, "A single-atom electron spin qubit in silicon," *Nature* **489**, 541 (2012).
- ¹⁶J. J. Pla, K. Y. Tan, J. P. Dehollain, W. H. Lim, J. J. L. Morton, F. A. Zwanenburg, D. N. Jamieson, A. S. Dzurak, and A. Morello, "High-fidelity readout and control of a nuclear spin qubit in silicon," *Nature* **496**, 334 (2013).
- ¹⁷M. T. Mądzik, A. Laucht, F. E. Hudson, A. M. Jakob, B. C. Johnson, D. N. Jamieson, K. M. Itoh, A. S. Dzurak, and A. Morello, "Conditional quantum operation of two exchange-coupled single-donor spin qubits in a MOS-compatible silicon device," *Nat. Commun.* **12**, 181 (2021).
- ¹⁸R. G. Clark, R. Brenner, T. M. Buehler, V. Chan, N. J. Curson, A. S. Dzurak, E. Gauja, H. S. Goan, A. D. Greentree, T. Hallam, A. R. Hamilton, L. C. L. Hollenberg, D. N. Jamieson, J. C. McCallum, G. J. Milburn, J. L. O'Brien, L. Oberbeck, C. I. Pakes, S. D. Praver, D. J. Reilly, F. J. Ruess, S. R. Schofield, M. Y. Simmons, F. E. Stanley, R. P. Starrett, C. Wellard, and C. Yang, "Progress in silicon-based quantum computing," *Philos. Trans. R. Soc. London, Ser. A* **361**, 1451 (2003).
- ¹⁹D. N. Jamieson, C. Yang, T. Hopf, S. M. Hearne, C. I. Pakes, S. Praver, M. Mitic, E. Gauja, S. E. Andresen, F. E. Hudson, A. S. Dzurak, and R. G. Clark,

- "Controlled shallow single-ion implantation in silicon using an active substrate for sub-20-keV ions," *Appl. Phys. Lett.* **86**, 202101 (2005).
- ²⁰M. Y. Simmons, F. J. Ruess, K. E. J. Goh, T. Hallam, S. R. Schofield, L. Oberbeck, N. J. Curson, A. R. Hamilton, M. J. Butcher, R. G. Clark, and T. C. G. Reusch, "Scanning probe microscopy for silicon device fabrication," *Mol. Simul.* **31**, 505 (2005).
 - ²¹F. Ruess, W. Pok, T. C. Reusch, M. Butcher, K. E. Goh, L. Oberbeck, G. Scappucci, A. R. Hamilton, and M. Y. Simmons, "Realization of atomically controlled dopant devices in silicon," *Small* **3**, 563 (2007).
 - ²²M. Koch, J. G. Keizer, P. Pakkiam, D. Keith, M. G. House, E. Peretz, and M. Y. Simmons, "Spin read-out in atomic qubits in an all-epitaxial three-dimensional transistor," *Nat. Nanotechnol.* **14**, 137 (2019).
 - ²³Y. He, S. K. Gorman, D. Keith, L. Kranz, J. G. Keizer, and M. Y. Simmons, "A two-qubit gate between phosphorus donor electrons in silicon," *Nature* **571**, 371 (2019).
 - ²⁴A. Morello, J. J. Pla, P. Bertet, and D. N. Jamieson, "Donor spins in silicon for quantum technologies," *Adv. Quantum Technol.* **3**, 2000005 (2020).
 - ²⁵T. D. Ladd and M. S. Carroll, "Silicon qubits," in *Encyclopedia of Modern Optics*, 2nd ed., edited by B. D. Guenther and D. G. Steel (Elsevier, Oxford, 2018), pp. 467–477.
 - ²⁶X. Zhang, H.-O. Li, G. Cao, M. Xiao, G.-C. Guo, and G.-P. Guo, "Semiconductor quantum computation," *Nat. Sci. Rev.* **6**, 32 (2018).
 - ²⁷A. Chatterjee, P. Stevenson, S. De Franceschi, A. Morello, N. P. de Leon, and F. Kuemmeth, "Semiconductor qubits in practice," *Nat. Rev. Phys.* **3**, 157 (2021).
 - ²⁸B. Koiller, X. Hu, R. B. Capaz, A. S. Martins, and S. Das Sarma, "Silicon-based spin and charge quantum computation," *An. Acad. Bras. Ciênc.* **77**, 201 (2005).
 - ²⁹M. Usman, C. D. Hill, R. Rahman, G. Klimeck, M. Y. Simmons, S. Rogge, and L. C. L. Hollenberg, "Strain and electric field control of hyperfine interactions for donor spin qubits in silicon," *Phys. Rev. B* **91**, 245209 (2015).
 - ³⁰Y. Wang, A. Tankasala, L. C. L. Hollenberg, G. Klimeck, M. Y. Simmons, and R. Rahman, "Highly tunable exchange in donor qubits in silicon," *npj Quantum Inf.* **2**, 16008 (2016).
 - ³¹M. Veldhorst, H. G. J. Eenink, C. H. Yang, and A. S. Dzurak, "Silicon CMOS architecture for a spin-based quantum computer," *Nat. Commun.* **8**, 1766 (2017).
 - ³²M. A. Fogarty, K. W. Chan, B. Hensen, W. Huang, T. Tanttu, C. H. Yang, A. Laucht, M. Veldhorst, F. E. Hudson, K. M. Itoh, D. Culcer, T. D. Ladd, A. Morello, and A. S. Dzurak, "Integrated silicon qubit platform with single-spin addressability, exchange control and single-shot singlet-triplet readout," *Nat. Commun.* **9**, 4370 (2018).
 - ³³M. F. Gonzalez-Zalba, S. de Franceschi, E. Charbon, T. Meunier, M. Vinet, and A. S. Dzurak, "Scaling silicon-based quantum computing using CMOS technology: State-of-the-art, challenges and perspectives," *arXiv:2011.11753 [quant-ph]* (2020).
 - ³⁴R. P. Feynman, "There's plenty of room at the bottom: An invitation to enter a new field of physics," *Caltech Eng. Sci.* **23**, 22 (1960).
 - ³⁵R. P. Feynman, "Simulating physics with computers," *Int. J. Theor. Phys.* **21**, 467 (1982).
 - ³⁶U. Meirav, M. A. Kastner, and S. J. Wind, "Single-electron charging and periodic conductance resonances in GaAs nanostructures," *Phys. Rev. Lett.* **65**, 771 (1990).
 - ³⁷B. E. Kane, "A silicon-based nuclear spin quantum computer," *Nature* **393**, 133 (1998).
 - ³⁸A. Morello, C. Escott, H. Huebl, L. Willems van Beveren, L. Hollenberg, D. Jamieson, A. Dzurak, and R. Clark, "Architecture for high-sensitivity single-shot readout and control of the electron spin of individual donors in silicon," *Phys. Rev. B* **80**, 081307 (2009).
 - ³⁹A. Morello, J. J. Pla, F. A. Zwanenburg, K. W. Chan, K. Y. Tan, H. Huebl, M. Möttönen, C. D. Nugroho, C. Yang, J. A. Van Donkelaar, A. D. C. Alves, D. N. Jamieson, C. C. Escott, L. C. L. Hollenberg, R. G. Clark, and A. S. Dzurak, "Single-shot readout of an electron spin in silicon," *Nature* **467**, 687 (2010).
 - ⁴⁰L. A. Tracy, T. M. Lu, N. C. Bishop, G. A. Ten Eyck, T. Pluym, J. R. Wendt, M. P. Lilly, and M. S. Carroll, "Electron spin lifetime of a single antimony donor in silicon," *Appl. Phys. Lett.* **103**, 143115 (2013).
 - ⁴¹S. J. Angus, A. J. Ferguson, A. S. Dzurak, and R. G. Clark, "A silicon radio-frequency single electron transistor," *Appl. Phys. Lett.* **92**, 112103 (2008).
 - ⁴²H. Huebl, C. D. Nugroho, A. Morello, C. C. Escott, M. A. Eriksson, C. Yang, D. N. Jamieson, R. G. Clark, and A. S. Dzurak, "Electron tunnel rates in a donor-silicon single electron transistor hybrid," *Phys. Rev. B* **81**, 235318 (2010).
 - ⁴³F. A. Mohiyaddin, R. Rahman, R. Kalra, G. Klimeck, L. C. L. Hollenberg, J. J. Pla, A. S. Dzurak, and A. Morello, "Noninvasive spatial metrology of single-atom devices," *Nano Lett.* **13**, 1903 (2013).
 - ⁴⁴B. Koiller, X. Hu, and S. Das Sarma, "Exchange in silicon-based quantum computer architecture," *Phys. Rev. Lett.* **88**, 027903 (2001).
 - ⁴⁵C. J. Wellard and L. C. L. Hollenberg, "Donor electron wave functions for phosphorus in silicon: Beyond effective-mass theory," *Phys. Rev. B* **72**, 085202 (2005).
 - ⁴⁶J. Salfi, J. A. Mol, R. Rahman, G. Klimeck, M. Y. Simmons, L. C. L. Hollenberg, and S. Rogge, "Spatially resolving valley quantum interference of a donor in silicon," *Nat. Mater.* **13**, 605 (2014).
 - ⁴⁷J. K. Gamble, N. T. Jacobson, E. Nielsen, A. D. Baczewski, J. E. Moussa, I. Montañó, and R. P. Muller, "Multivalley effective mass theory simulation of donors in silicon," *Phys. Rev. B* **91**, 235318 (2015).
 - ⁴⁸J. T. Muhonen, J. P. Dehollain, A. Laucht, F. E. Hudson, R. Kalra, T. Sekiguchi, K. M. Itoh, D. N. Jamieson, J. C. McCallum, A. S. Dzurak, and A. Morello, "Storing quantum information for 30 seconds in a nanoelectronic device," *Nat. Nanotechnol.* **9**, 986 (2014).
 - ⁴⁹J. M. Elzerman, R. Hanson, L. H. Willems van Beveren, B. Witkamp, L. M. K. Vandersypen, and L. P. Kouwenhoven, "Single-shot read-out of an individual electron spin in a quantum dot," *Nature* **430**, 431 (2004).
 - ⁵⁰https://www.st-andrews.ac.uk/physics/quvis/simulations_html5/sims/bloch-sphere/blochsphere.html for Bloch Sphere Representation of Quantum States for a Spin 1/2 Particle, QuVis: The Quantum Mechanics Visualisation Project, University of St Andrews.
 - ⁵¹M. K. Bowman, "Pulsed methods in electron spin resonance," in *Encyclopedia of Analytical Chemistry* (American Cancer Society, 2010).
 - ⁵²E. L. Hahn, "Spin echoes," *Phys. Rev.* **80**, 580 (1950).
 - ⁵³I. I. Rabi, "Space quantization in a gyrating magnetic field," *Phys. Rev.* **51**, 652 (1937).
 - ⁵⁴N. F. Ramsey, "A molecular beam resonance method with separated oscillating fields," *Phys. Rev.* **78**, 695 (1950).
 - ⁵⁵A. M. Tyryshkin, J. J. L. Morton, S. C. Benjamin, A. Ardavan, G. A. D. Briggs, J. W. Ager, and S. A. Lyon, "Coherence of spin qubits in silicon," *J. Phys.: Condens. Matter* **18**, S783 (2006).
 - ⁵⁶X. Hu, R. de Sousa, and S. Das Sarma, "Decoherence and dephasing in spin-based solid state quantum computers," *arXiv:Cond-mat/0108339* (2001).
 - ⁵⁷L. M. K. Vandersypen and I. L. Chuang, "NMR techniques for quantum control and computation," *Rev. Mod. Phys.* **76**, 1037 (2005).
 - ⁵⁸G. Feher, "Electron spin resonance experiments on donors in silicon. I. Electronic structure of donors by the electron nuclear double resonance technique," *Phys. Rev.* **114**, 1219 (1959).
 - ⁵⁹V. B. Braginsky and F. Y. Khalili, "Quantum nondemolition measurements: The route from toys to tools," *Rev. Mod. Phys.* **68**, 1 (1996).
 - ⁶⁰A. M. Tyryshkin, S. Tojo, J. J. L. Morton, H. Riemann, N. V. Abrosimov, P. Becker, H.-J. Pohl, T. Schenkel, M. L. W. Thewalt, K. M. Itoh, and S. A. Lyon, "Electron spin coherence exceeding seconds in high-purity silicon," *Nat. Mater.* **11**, 143 (2012).
 - ⁶¹K. Saeedi, S. Simmons, J. Z. Salvail, P. Dluhy, H. Riemann, N. V. Abrosimov, P. Becker, H.-J. Pohl, J. J. L. Morton, and M. L. W. Thewalt, "Room-temperature quantum bit storage exceeding 39 minutes using ionized donors in silicon-28," *Science* **342**, 830 (2013).
 - ⁶²J. T. Muhonen, A. Laucht, S. Simmons, J. P. Dehollain, R. Kalra, F. E. Hudson, S. Freer, K. M. Itoh, D. N. Jamieson, J. C. McCallum, A. S. Dzurak, and A. Morello, "Quantifying the quantum gate fidelity of single-atom spin qubits in silicon by randomized benchmarking," *J. Phys.: Condens. Matter* **27**, 154205 (2015).
 - ⁶³J. P. Dehollain, J. T. Muhonen, R. Blume-Kohout, K. M. Rudinger, J. K. Gamble, E. Nielsen, A. Laucht, S. Simmons, R. Kalra, A. S. Dzurak, and A. Morello, "Optimization of a solid-state electron spin qubit using gate set tomography," *New J. Phys.* **18**, 103018 (2016).

- ⁶⁴X. Cai, "Quantum dephasing induced by non-Markovian random telegraph noise," *Sci. Rep.* **10**, 88 (2020).
- ⁶⁵S. Freer, S. Simmons, A. Laucht, J. T. Muhonen, J. P. Dehollain, R. Kalra, F. A. Mohiyaddin, F. E. Hudson, K. M. Itoh, J. C. McCallum, D. N. Jamieson, A. S. Dzurak, and A. Morello, "A single-atom quantum memory in silicon," *Quantum Sci. Technol.* **2**, 015009 (2017).
- ⁶⁶J. P. Dehollain, S. Simmons, J. T. Muhonen, R. Kalra, A. Laucht, F. Hudson, K. M. Itoh, D. N. Jamieson, J. C. McCallum, A. S. Dzurak, and A. Morello, "Bell's inequality violation with spins in silicon," *Nat. Nanotechnol.* **11**, 242 (2016).
- ⁶⁷J. S. Bell, "On the Einstein Podolsky Rosen paradox," *Phys. Phys. Fiz.* **1**, 195 (1964).
- ⁶⁸J. Clauser, M. A. Horne, A. Shimony, and R. A. Holt, "Proposed experiment to test local hidden-variable theories," *Phys. Rev. Lett.* **23**, 880 (1969).
- ⁶⁹J. P. Dehollain, J. T. Muhonen, K. Y. Tan, A. Saraiva, D. N. Jamieson, A. S. Dzurak, and A. Morello, "Single-shot readout and relaxation of singlet and triplet states in exchange-coupled, ³¹P electron spins in silicon," *Phys. Rev. Lett.* **112**, 236801 (2014).
- ⁷⁰A. Laucht, J. T. Muhonen, F. A. Mohiyaddin, R. Kalra, J. P. Dehollain, S. Freer, F. E. Hudson, M. Veldhorst, R. Rahman, G. Klimeck, K. M. Itoh, D. N. Jamieson, J. C. McCallum, A. S. Dzurak, and A. Morello, "Electrically controlling single-spin qubits in a continuous microwave field," *Sci. Adv.* **1**, e1500022 (2015).
- ⁷¹A. Laucht, R. Kalra, S. Simmons, J. P. Dehollain, J. T. Muhonen, F. A. Mohiyaddin, S. Freer, F. E. Hudson, K. M. Itoh, D. N. Jamieson, J. C. McCallum, A. S. Dzurak, and A. Morello, "A dressed spin qubit in silicon," *Nat. Nanotechnol.* **12**, 61 (2017).
- ⁷²B. R. Mollow, "Power spectrum of light scattered by two-level systems," *Phys. Rev.* **188**, 1969 (1969).
- ⁷³C. H. Bennett and D. P. DiVincenzo, "Quantum information and computation," *Nature* **404**, 247 (2000).
- ⁷⁴J. J. Pla, F. A. Mohiyaddin, K. Y. Tan, J. P. Dehollain, R. Rahman, G. Klimeck, D. N. Jamieson, A. S. Dzurak, and A. Morello, "Coherent control of a single, ²⁹Si nuclear spin qubit," *Phys. Rev. Lett.* **113**, 246801 (2014).
- ⁷⁵M. T. Mądzik, S. Asaad, A. Youssry, B. Joecker, K. M. Rudinger, E. Nielsen, K. C. Young, T. J. Proctor, A. D. Baczewski, A. Laucht, V. Schmitt, F. E. Hudson, K. M. Itoh, A. M. Jakob, B. C. Johnson, D. N. Jamieson, A. S. Dzurak, C. Ferrie, R. Blume-Kohout, and A. Morello, "Precision tomography of a three-qubit electron–nuclear quantum processor in silicon," *arXiv:2106.03082* [quant-ph] (2021).
- ⁷⁶S. Asaad, V. Mourik, B. Joecker, M. A. I. Johnson, A. D. Baczewski, H. R. Firgau, M. T. Mądzik, V. Schmitt, J. J. Pla, F. E. Hudson, K. M. Itoh, J. C. McCallum, A. S. Dzurak, A. Laucht, and A. Morello, "Coherent electrical control of a single high-spin nucleus in silicon," *Nature* **579**, 205 (2020).
- ⁷⁷N. Bloembergen, "National Academy of Sciences," *Science* **133**, 1363 (1961).
- ⁷⁸V. Mourik, S. Asaad, H. Firgau, J. J. Pla, C. Holmes, G. J. Milburn, J. C. McCallum, and A. Morello, "Exploring quantum chaos with a single nuclear spin," *Phys. Rev. E* **98**, 042206 (2018).
- ⁷⁹D. P. Franke, M. P. D. Pflüger, P.-A. Mortemousque, K. M. Itoh, and M. S. Brandt, "Quadrupolar effects on nuclear spins of neutral arsenic donors in silicon," *Phys. Rev. B* **93**, 161303 (2016).
- ⁸⁰C. C. Lo, S. Simmons, R. Lo Nardo, C. D. Weis, A. M. Tyryshkin, J. Meijer, D. Rogalla, S. A. Lyon, J. Bokor, T. Schenkel, and J. J. L. Morton, "Stark shift and field ionization of arsenic donors in ²⁸Si-silicon-on-insulator structures," *Appl. Phys. Lett.* **104**, 193502 (2014).
- ⁸¹J. Z. Salvail, P. Dluhy, K. J. Morse, M. Szech, K. Saeedi, J. Huber, H. Riemann, N. V. Abrosimov, P. Becker, H.-J. Pohl, and M. L. W. Thewalt, "Optically enabled magnetic resonance study of, ⁷⁵As and, ¹²¹Sb in, ²⁸Si," *Phys. Rev. B* **92**, 195203 (2015).
- ⁸²A. J. Sigillito, A. M. Tyryshkin, T. Schenkel, A. A. Houck, and S. A. Lyon, "All-electric control of donor nuclear spin qubits in silicon," *Nat. Nanotechnol.* **12**, 958 (2017).
- ⁸³T. J. Z. Stock, O. Warschkow, P. C. Constantinou, J. Li, S. Fearn, E. Crane, E. V. S. Hofmann, A. Kölker, D. R. McKenzie, S. R. Schofield, and N. J. Curson, "Atomic-scale patterning of arsenic in silicon by scanning tunneling microscopy," *ACS Nano* **14**, 3316 (2020).
- ⁸⁴M. H. Mohammady, G. W. Morley, and T. S. Monteiro, "Bismuth qubits in silicon: The role of EPR cancellation resonances," *Phys. Rev. Lett.* **105**, 067602 (2010).
- ⁸⁵G. Wolfowicz, A. M. Tyryshkin, R. E. George, H. Riemann, N. V. Abrosimov, P. Becker, H.-J. Pohl, M. L. W. Thewalt, S. A. Lyon, and J. J. L. Morton, "Atomic clock transitions in silicon-based spin qubits," *Nat. Nanotechnol.* **8**, 561 (2013).
- ⁸⁶W.-L. Ma, G. Wolfowicz, S.-S. Li, J. J. L. Morton, and R.-B. Liu, "Classical nature of nuclear spin noise near clock transitions of Bi donors in silicon," *Phys. Rev. B* **92**, 161403 (2015).
- ⁸⁷D. Holmes, W. I. L. Lawrie, B. C. Johnson, A. Asadpoordarvish, J. C. McCallum, D. R. McCamey, and D. N. Jamieson, "Activation and electron spin resonance of near-surface implanted bismuth donors in silicon," *Phys. Rev. Mater.* **3**, 083403 (2019).
- ⁸⁸J. F. Ziegler, M. D. Ziegler, and J. P. Biersack, "SRIM—The stopping and range of ions in matter (2010)," *Nucl. Instrum. Methods Phys. Res., Sect. B* **268**, 1818 (2010).
- ⁸⁹M. Posselt, "Crystal-trim and its application to investigations on channeling effects during ion implantation," *Radiat. Eff. Defects Solids* **199A**, 87.
- ⁹⁰H. F. Wilson, N. A. Marks, D. R. McKenzie, and K. H. Lee, "Molecular dynamics simulations of ion implantation for the fabrication of a solid-state quantum computer," *Nucl. Instrum. Methods Phys. Res., Sect. B* **215**, 99 (2004).
- ⁹¹O. Lehtinen, B. Naydenov, P. Börner, K. Melentjevic, C. Müller, L. P. McGuinness, S. Pezzagna, J. Meijer, U. Kaiser, and F. Jelezko, "Molecular dynamics simulations of shallow nitrogen and silicon implantation into diamond," *Phys. Rev. B* **93**, 035202 (2016).
- ⁹²J. McCallum, M. L. Dunn, and E. Gauja, "Ion implantation through thin silicon dioxide layers for Si-based solid-state quantum computer device development," *MRS Online Proc. Library* **1074**, 10741205 (2008).
- ⁹³T. Schenkel, J. A. Liddle, A. Persaud, A. M. Tyryshkin, S. A. Lyon, R. de Sousa, K. B. Whaley, J. Bokor, J. Shangquan, and I. Chakarov, "Electrical activation and electron spin coherence of ultralow dose antimony implants in silicon," *Appl. Phys. Lett.* **88**, 112101 (2006).
- ⁹⁴H. Bracht, "Advanced dopant and self-diffusion studies in silicon," *Nucl. Instrum. Methods Phys. Res., Sect. B* **253**, 105 (2006).
- ⁹⁵P. Kringhøj, A. N. Larsen, and S. Y. Shirayev, "Diffusion of Sb in strained and relaxed Si and SiGe," *Phys. Rev. Lett.* **76**, 3372 (1996).
- ⁹⁶Y. Ishikawa, K. Yazaki, and I. Nakamichi, "The diffusion of bismuth in silicon," *Jpn. J. Appl. Phys., Part 1* **28**, 1272 (1989).
- ⁹⁷Y. Ishikawa, I. Kobayashi, and I. Nakamichi, "Oxidation-retarded diffusion of bismuth in silicon," *Jpn. J. Appl. Phys., Part 2* **29**, L1929 (1990).
- ⁹⁸R. Duffy, T. Dao, Y. Tammimga, K. van der Tak, F. Roozeboom, and E. Augendre, "Groups III and V impurity solubilities in silicon due to laser, flash, and solid-phase-epitaxial-regrowth anneals," *Appl. Phys. Lett.* **89**, 071915 (2006).
- ⁹⁹C. D. Weis, C. C. Lo, V. Lang, A. M. Tyryshkin, R. E. George, K. M. Yu, J. Bokor, S. A. Lyon, J. J. L. Morton, and T. Schenkel, "Electrical activation and electron spin resonance measurements of implanted bismuth in isotopically enriched silicon-28," *Appl. Phys. Lett.* **100**, 172104 (2012).
- ¹⁰⁰T. Shinada, T. Kurosawa, H. Nakayama, Y. Zhu, M. Hori, and I. Ohdomari, "A reliable method for the counting and control of single ions for single-dopant controlled devices," *Nanotechnology* **19**, 345202 (2008).
- ¹⁰¹M. Hori, K. Taira, A. Komatsubara, K. Kumagai, Y. Ono, T. Tani, T. Endoh, and T. Shinada, "Reduction of threshold voltage fluctuation in field-effect transistors by controlling individual dopant position," *Appl. Phys. Lett.* **101**, 013503 (2012).
- ¹⁰²T. Shinada, A. Ishikawa, M. Fujita, K. Yamashita, and I. Ohdomari, "Influence of secondary electron detection efficiency on controllability of dopant ion number in single ion implantation," *Jpn. J. Appl. Phys.* **38**, 3419 (1999).
- ¹⁰³B. E. Fischer, M. Heiß, and M. Cholewa, "About the art to shoot with single ions," *Nucl. Instrum. Methods Phys. Res., Sect. B* **210**, 285 (2003).
- ¹⁰⁴T. Schenkel, C. D. Weis, C. C. Lo, A. Persaud, I. Chakarov, D. H. Schneider, and J. Bokor, "Deterministic doping and the exploration of spin qubits," *AIP Conf. Proc.* **1640**, 124 (2015).
- ¹⁰⁵N. Yoshiyasu, S. Takahashi, M.-a. Shibata, H. Shimizu, K. Nagata, N. Nakamura, M. Tona, M. Sakurai, C. Yamada, and S. Ohtani, "Demonstrative

- experiment for single-ion implantation technique using highly charged ions," *Jpn. J. Appl. Phys., Part 1* **45**, 995 (2006).
- ¹⁰⁶E. Bielejec, J. A. Seamons, and M. S. Carroll, "Single ion implantation for single donor devices using Geiger mode detectors," *Nanotechnology* **21**, 085201 (2010).
- ¹⁰⁷J. A. Seamons, E. Bielejec, M. S. Carroll, and K. D. Childs, "Room temperature single ion detection with Geiger mode avalanche diode detectors," *Appl. Phys. Lett.* **93**, 043124 (2008).
- ¹⁰⁸M. Singh, J. L. Pacheco, D. Perry, E. Garratt, G. Ten Eyck, N. C. Bishop, J. R. Wendt, R. P. Manginell, J. Dominguez, T. Pluym, D. R. Luhman, E. Bielejec, M. P. Lilly, and M. S. Carroll, "Electrostatically defined silicon quantum dots with counted antimony donor implants," *Appl. Phys. Lett.* **108**, 062101 (2016).
- ¹⁰⁹J. L. Pacheco, M. Singh, D. L. Perry, J. R. Wendt, G. Ten Eyck, R. P. Manginell, T. Pluym, D. R. Luhman, M. P. Lilly, M. S. Carroll, and E. Bielejec, "Ion implantation for deterministic single atom devices," *Rev. Sci. Instrum.* **88**, 123301 (2017).
- ¹¹⁰C. Yin, M. Rancic, G. G. de Boo, N. Stavrias, J. C. McCallum, M. J. Sellars, and S. Rogge, "Optical addressing of an individual erbium ion in silicon," *Nature* **497**, 91 (2013).
- ¹¹¹Q. Zhang, G. Hu, G. G. de Boo, M. Rančić, B. C. Johnson, J. C. McCallum, J. Du, M. J. Sellars, C. Yin, and S. Rogge, "Single rare-earth ions as atomic-scale probes in ultrascaled transistors," *Nano Lett.* **19**, 5025 (2019).
- ¹¹²A. Batra, C. D. Weis, J. Reijonen, A. Persaud, T. Schenkel, S. Cabrini, C. C. Lo, and J. Bokor, "Detection of low energy single ion impacts in micron scale transistors at room temperature," *Appl. Phys. Lett.* **91**, 193502 (2007).
- ¹¹³T. Shinada, M. Hori, K. Taira, T. Endoh, and I. Ohdomari, "Recent advance in single-ion implantation method for single-dopant devices," in *2009 International Workshop on Junction Technology* (IEEE, 2009), pp. 96–99.
- ¹¹⁴B. C. Johnson, G. C. Tettamanzi, A. D. C. Alves, S. Thompson, C. Yang, J. Verduijn, J. A. Mol, R. Wacquez, M. Vinet, M. Sanquer, S. Rogge, and D. N. Jamieson, "Drain current modulation in a nanoscale field-effect-transistor channel by single dopant implantation," *Appl. Phys. Lett.* **96**, 264102 (2010).
- ¹¹⁵K. Groot-Berning, T. Kornher, G. Jacob, F. Stopp, S. T. Dawkins, R. Kolesov, J. Wrachtrup, K. Singer, and F. Schmidt-Kaler, "Deterministic single-ion implantation of rare-earth ions for nanometer-resolution color-center generation," *Phys. Rev. Lett.* **123**, 106802 (2019).
- ¹¹⁶W. Schnitzler, N. M. Linke, R. Fickler, J. Meijer, F. Schmidt-Kaler, and K. Singer, "Deterministic ultracold ion source targeting the Heisenberg limit," *Phys. Rev. Lett.* **102**, 070501 (2009).
- ¹¹⁷G. Jacob, K. Groot-Berning, S. Wolf, S. Ulm, L. Couturier, S. T. Dawkins, U. G. Poschinger, F. Schmidt-Kaler, and K. Singer, "Transmission microscopy with nanometer resolution using a deterministic single ion source," *Phys. Rev. Lett.* **117**, 043001 (2016).
- ¹¹⁸J. Meijer, T. Vogel, B. Burchard, I. W. Rangelow, L. Bischoff, J. Wrachtrup, M. Domhan, F. Jelezko, W. Schnitzler, S. A. Schulz, K. Singer, and F. Schmidt-Kaler, "Concept of deterministic single ion doping with sub-nm spatial resolution," *Appl. Phys. A* **83**, 321 (2006).
- ¹¹⁹M. Ilg, C. D. Weis, J. Schwartz, A. Persaud, Q. Ji, C. C. Lo, J. Bokor, A. Hegyi, E. Guliyev, I. W. Rangelow, and T. Schenkel, "Improved single ion implantation with scanning probe alignment," *J. Vac. Sci. Technol. B* **30**, 06FD04 (2012).
- ¹²⁰T. Matsukawa, T. Fukai, S. Suzuki, K. Hara, M. Koh, and I. Ohdomari, "Development of single-ion implantation—Controllability of implanted ion number," *Appl. Surf. Sci.* **117–118**, 677 (1997).
- ¹²¹V. Millar, C. I. Pakes, A. Cimmino, D. Brett, D. N. Jamieson, S. Praver, C. J. Yang, B. Rout, R. P. McKinnon, A. S. Dzura, and R. G. Clark, "Nanoscale fabrication using single-ion impacts," *Smart Mater. Struct.* **11**, 686 (2002).
- ¹²²C. D. Hill, E. Peretz, S. J. Hile, M. G. House, M. Fuechsle, S. Rogge, M. Y. Simmons, and L. C. L. Hollenberg, "A surface code quantum computer in silicon," *Sci. Adv.* **1**, e1500707 (2015).
- ¹²³R. Kalra, A. Laucht, C. D. Hill, and A. Morello, "Robust two-qubit gates for donors in silicon controlled by hyperfine interactions," *Phys. Rev. X* **4**, 021044 (2014).
- ¹²⁴G. Tosi, F. A. Mohiyaddin, V. Schmitt, S. Tenberg, R. Rahman, G. Klimeck, and A. Morello, "Silicon quantum processor with robust long-distance qubit couplings," *Nat. Commun.* **8**(1), 450 (2017).
- ¹²⁵G. Tosi, F. A. Mohiyaddin, H. Huebl, and A. Morello, "Circuit-quantum electrodynamics with direct magnetic coupling to single-atom spin qubits in isotopically enriched ^{28}Si ," *AIP Adv.* **4**, 087122 (2014).
- ¹²⁶G. Tosi, F. A. Mohiyaddin, S. Tenberg, A. Laucht, and A. Morello, "Robust electric dipole transition at microwave frequencies for nuclear spin qubits in silicon," *Phys. Rev. B* **98**, 075313 (2018).
- ¹²⁷L. C. L. Hollenberg, A. D. Greentree, A. G. Fowler, and C. J. Wellard, "Two-dimensional architectures for donor-based quantum computing," *Phys. Rev. B* **74**, 045311 (2006).
- ¹²⁸J. O'Gorman, N. H. Nickerson, P. Ross, J. J. Morton, and S. C. Benjamin, "A silicon-based surface code quantum computer," *npj Quantum Inf.* **2**, 15019 (2016).
- ¹²⁹T. Schenkel, C. C. Lo, C. D. Weis, J. Bokor, A. M. Tyryshkin, and S. A. Lyon, "A spin quantum bit architecture with coupled donors and quantum dots in silicon," *arXiv:1110.2228* [cond-mat] (2011).
- ¹³⁰M. Urdampilleta, A. Chatterjee, C. C. Lo, T. Kobayashi, J. Mansir, S. Barraud, A. C. Betz, S. Rogge, M. F. Gonzalez-Zalba, and J. J. L. Morton, "Charge dynamics and spin blockade in a hybrid double quantum dot in silicon," *Phys. Rev. X* **5**, 031024 (2015).
- ¹³¹P. Harvey-Collard, N. T. Jacobson, M. Rudolph, J. Dominguez, G. A. T. Eyck, J. R. Wendt, T. Pluym, J. K. Gamble, M. P. Lilly, M. Pioro-Ladrière, and M. S. Carroll, "Coherent coupling between a quantum dot and a donor in silicon," *Nat. Commun.* **8**, 1029 (2017).
- ¹³²K. J. Morse, R. J. S. Abraham, A. DeAbreu, C. Bowness, T. S. Richards, H. Riemann, N. V. Abrosimov, P. Becker, H.-J. Pohl, M. L. W. Thewalt, and S. Simmons, "A photonic platform for donor spin qubits in silicon," *Sci. Adv.* **3**, e1700930 (2017).
- ¹³³M. Friesen, A. Biswas, X. Hu, and D. Lidar, "Efficient multiqubit entanglement via a spin bus," *Phys. Rev. Lett.* **98**, 230503 (2007).
- ¹³⁴S. Oh, Y.-P. Shim, J. Fei, M. Friesen, and X. Hu, "Resonant adiabatic passage with three qubits," *Phys. Rev. A* **87**, 022332 (2013).
- ¹³⁵F. A. Mohiyaddin, R. Kalra, A. Laucht, R. Rahman, G. Klimeck, and A. Morello, "Transport of spin qubits with donor chains under realistic experimental conditions," *Phys. Rev. B* **94**, 045314 (2016).
- ¹³⁶M. J. Calderón, B. Koiller, X. Hu, and S. D. Sarma, "Quantum control of donor electrons at the Si-SiO₂ interface," *Phys. Rev. Lett.* **96**, 096802 (2006).
- ¹³⁷L. Trifunovic, F. L. Pedrocchi, and D. Loss, "Long-distance entanglement of spin qubits via ferromagnet," *Phys. Rev. X* **3**, 041023 (2013).
- ¹³⁸V. Srinivasa, H. Xu, and J. Taylor, "Tunable spin-qubit coupling mediated by a multi-electron quantum dot," *Phys. Rev. Lett.* **114**, 226803 (2015).
- ¹³⁹F. K. Malinowski, F. Martins, T. B. Smith, S. D. Bartlett, A. C. Doherty, P. D. Nissen, S. Fallahi, G. C. Gardner, M. J. Manfra, C. M. Marcus, and F. Kuemmeth, "Spin of a multi-electron quantum dot and its interaction with a neighboring electron," *Phys. Rev. X* **8**, 011045 (2018).
- ¹⁴⁰X. Croot, S. Pauka, J. Watson, G. Gardner, S. Fallahi, M. Manfra, and D. Reilly, "Device architecture for coupling spin qubits via an intermediate quantum state," *Phys. Rev. Appl.* **10**, 044058 (2018).